Journal Pre-proof

A novel approach to reduce fan rotor blades stress in case of resonance due to inlet flow distortion by means of piezoelectric actuators

Andrea Rossi, Fabio Botta, Ambra Giovannelli, Nicola Pio Belfiore

PII: S0022-460X(23)00002-0
DOI: https://doi.org/10.1016/j.jsv.2023.117552
Reference: YJSVI 117552

To appear in: *Journal of Sound and Vibration*

Received date : 21 September 2022
Revised date : 20 December 2022
Accepted date : 4 January 2023

Please cite this article as: A. Rossi, F. Botta, A. Giovannelli et al., A novel approach to reduce fan rotor blades stress in case of resonance due to inlet flow distortion by means of piezoelectric actuators, *Journal of Sound and Vibration* (2023), doi: https://doi.org/10.1016/j.jsv.2023.117552.

A novel approach to reduce fan rotor blades stress in case of resonance due to inlet flow distortion by means of piezoelectric actuators

Andrea Rossi[a]*, Fabio Botta[a], Ambra Giovannelli[a], Nicola Pio Belfiore[a]

[a] *Department of Industrial, Electronic and Mechanical Engineering*
University of Roma Tre
Via della Vasca Navale, 79 - Rome, Italy

Abstract

Resonant vibration condition involves a drop in the life-cycle of the components and is one of the main causes of high cycle fatigue failure (HCF) in turbomachinery blades. As a consequence vibration damping techniques play a key role for turbomachinery designers. Even though resonant vibration conditions can be identified by means of the Singh's Advanced Frequency Evaluation (SAFE) diagram at the design level, not all resonant conditions can be avoided. Among these methods, systems of piezoelectric (PZT) actuators can be tuned to actively damp the vibrations caused by resonant excitations. In this work, an analytical model was developed to identify the optimal voltage distribution that maximises the reduction in blade stress. The model considers the flexural-torsional-extensional deformations coupling due to the pre-twisting, non-constant cross-section and inertial loads of the rotating blades. A typical case was examined to demonstrate the effectiveness of the proposed method, which involved vibration induced by inlet flow distortion in an axial fan stage coupled with a three-strut front frame. A decoupled approach based on Computational Fluid Dynamics (CFD) and Finite Element Analysis (FEA) simulations was used to evaluate the aerodynamic loads and to numerically validate the optimal voltage distribution on the PZT actuator pairs. The results show that the proposed method

*Corresponding author
Email address: andrea.rossi@uniroma3.it (Andrea Rossi[a])

alleviates the effects of the resonant response to an inlet flow distortion on a fan integrally bladed disc (blisk) and the optimal voltage distribution predicted by the model is the one that achieves the highest blade stress mitigation.

Keywords: Forced response, inlet distortion, active vibration damping, piezoelectric actuator

Nomenclature	
A	blade cross-section area
d_{31}	piezoelectric coefficient
E_a	Young's modulus of the piezoelectric material
E_b	Young's modulus of the beam
E	Young's modulus of the blade
t_a	thickness of the piezoelectric material
t_b	thickness of the beam
t	thickness of the blade
b	width of the beam
η_{le}, η_{te}	distance between the elastic center and respectively the leading and trailing edge
I_i	second moment of area with respect to i axis
L	blade length in radial direction
M_a	piezoelectric bending moment
V	voltage applied to the piezoelectric plates
α	flexural deflection of the elastic axis in η- direction
γ	flexural deflection of the elastic axis in ζ- direction
χ_i	curvature with respect to i- axis
$\theta_\eta, \theta_\zeta$	rotations around η, ζ axes
$\theta_x, \theta_y, \theta_z$	rotations around x, y, z axes
$\sim$	virtual quantity
β	blade twist angle
δL_e	virtual works of elastic forces
δL_{in}	virtual works of inertial forces
δL_p	virtual works of piezoelectric forces
δL_a	virtual works of aerodynamic forces
$\xi = \frac{x}{L}$	dimensionless radial coordinate
ξ_1	dimensionless coordinate of the left edge of the piezoelectric actuator
ξ_2	dimensionless coordinate of the right edge of the piezoelectric actuator
p_x, p_η, p_ζ	inertial forces resultant in x, η, ζ directions
P_a	pressure acting on the blade surfaces due to the aerodynamic loads
p_a	resultant of the aerodynamic pressure (acting on the airfoil's frontier)
q_a	resultant of the moments due to the aerodynamic loads
q_x, q_η, q_ζ	inertial moments resultant in x, η, ζ direction
(u, v, w)	displacements in x, y, z components
M_x, M_η, M_ζ	internal elastic moments
ω_i	i-th natural angular frequency

1. Introduction

The variable nature of the aerodynamic loads acting on the rotor blades of a gas turbine during operation entails the possibility to excite one or more eigenmodes of an integrally bladed disc (blisk). The flow in a turbomachine is intrinsically non-stationary and if marked periodic flow disturbances match an eigenfrequency of a blade, then severe vibration may occur if the aerodynamic and structural damping are too low. The frequency of the disturbances is proportional to the rotor speed and it is denoted by the engine order (EO).

Under resonance conditions, the magnitude of the blade stress may exceed the fatigue strength and several fatigue cycles may occur until the resonance is overcome. Furthermore, the design of gas turbine blades aims to increase the machine's performance by reducing the clearances (i.e. the narrower axial gap between rotor and stator) and weight (i.e. lightweight materials, slender profiles). As a consequence the blades are more susceptible to a high level of vibrations [1–3].

Since higher vibration levels are involved at the lowest eigenmodes, low EO disturbances may be detrimental. Such excitations are mainly experienced by blades in turbine stages but also fan and compressor stages because of inlet flow distortions generated by the presence of struts, non-uniformity of inlet ducts, inlet guide vanes, etc. [4, 5]. Several reports in the literature have focused on the unsteady flow in fans and compressors in the case of inlet distortions. Sharma et al. [6] analysed the unsteady flow generated by 1EO inlet total pressure distortion in a high by-pass fan. Liu et al. [7] investigated the effects of total pressure and total temperature inlet distortions on the flow field in a NASA 37 compressor. Furthermore, Yamamoto and Ng [8] carried out numerical simulations to study the circumferential distortion due to the upstream struts in a supersonic inlet of a fan.

Even though all the resonant conditions of a blisk within its operating speed range can be identified at the design level, it is impossible to remove all the resonances by redesigning the geometry of the blade, because such modifications may significantly worsen the aerodynamic efficiency and increase the associated costs. More convenient approaches are based on increasing the structural damping of the component by employing passive or active systems. Passive damping systems such as friction dampers and shrouded blades are well-consolidated technologies in the turbomachinery field because they are effective and easy to implement. Such dampers are most effective at low frequencies but are inherently subject to wear, and the friction dampers may lose their effectiveness as the operation cycles grow. The main disadvantage of shrouded blades is the loss of the aerodynamic efficiency of the blade profiles, i.e. due to the presence of the lacing wire [9, 10].

Notably, the recent advancements in the smart materials have led to the development of passive and active damping systems in numerous engineering applications. Such materials provide the unique ability to modulate their mechanical behaviour through an external stimulus which can be represented by stress, electric or magnetic fields, temperature variations, etc.

For instance, plasma actuators were used for aeroelastic control of compressor cascades in [11], Garafolo and McHugh investigated shape memory alloys (SMA) as an active suppression system to mitigate aeroelastic flutter [12]. The implementation of piezoelectric materials has been widely investigated for several applications including: energy harvesting [13–15], aeroelastic control of wings [16, 17] or hybrid piezoelectric motors [18].

Concerning the particular application of vibration damping in fan and low compressor rotor blades, the most prominent smart materials are piezoelectric ceramics (PZT) because they exhibit a large bandwidth, fast response, high resolution, relatively high Curie temperature (300 - 350°C) and low manufacturing costs. PZT shunts and resonant shunts [19–21] have been used in turbomachinery applications and may achieve significant vibration attenuation, but their effectiveness is considerably reduced as the shaft speed increases. Moreover, such systems can be tailored to a specific natural frequency of the blade and, if the resonance condition changes, the PZT shunts may be ineffective.

Damping techniques based on active piezoelectric systems generally offer better performance than passive ones and active systems demonstrate the capability to tune the actuator action under each resonance condition.

However, only a few studies have explored active piezoelectric damping systems in turbomachinery blades. Goltz [22] used piezoelectric actuators to control the vibration in an axial compressor. Choi [23, 24] implemented an active device to damp fan blades vibration and Provenza [25] reported on the wireless application of PZT elements control in rotating plates. Importantly, the efficiency of PZT active systems is greatly affected by the actuator placement. Earlier studies investigating optimal actuator positioning to efficiently damp single mode excitations were performed by [26] and [27].

In the present work, a method presented in a previous paper ([28]) is generalised and extended to the case of real rotating blades. The differences with previous work are very significant both physically and methodologically. In fact, a non-rotating cantilever beam with a constant cross-section was treated in the former work. Conversely, actual turbomachinery blades are non-symmetrical, pre-twisted and have variable cross-sections for aerodynamic efficiency reasons, and they are also subjected to inertial loads due to rotation. Non-symmetry implies non-coincidence between the centre of shear and the centre of the section, resulting in the flexural-torsional coupling, so that bending cannot be treated individually, but it inevitably must be treated together with torsion. The differential equations of equilibrium have non-constant coefficients because of the pre-twist and the variability of the section along the radius. The presence of the inertial loads produces an additional coupling between the flexural and extensional deformations, which requires the considerations of the nonlinear part of the deformation to properly account for the variability of the eigenfrequencies with the angular velocity. To demonstrate the effectiveness of the proposed model, it was applied to a typical case of vibrations induced in an axial fan stage with a three-strut front frame. The forced response of the tuned fan rotor blisk is assessed using FEA and CFD simulations using a decoupled approach [29], from which the aerodynamic loads are characterised by low EOs because of the presence of upstream struts. As a consequence, some low natural frequencies of the blisk are excited within the operating speed of the fan. In this regard, each blade is covered with PZT pairs (PP) on its pressure and suction surfaces and a new analytical model is developed to find the optimal voltage distribution, i.e., the distribution that leads to the lowest level of blade stress is analytically identified for each blade resonance. The numerical simulations show that the optimal voltage distribution according to the analytical model results in the highest blade stress mitigation. Furthermore, the outcomes reveal that the method ensures high blade stress mitigation for each resonance condition and show the good robustness of the proposed strategy because there are several configurations close to the optimal one that do not undermine the stress relief effectiveness. The results obtained here are not restricted to the considered type of blade but are general and can be applied to all turbomachinery blades. Particularly, these results are relevant since it may be possible to automatically control the electric potential delivered to each PP to adapt their action to the excited eigenmode. In this regard, a novel system based on wireless power transfer has been developed to control PZT actuators mounted on rotating blades. Currently, the prototype wireless system is being tested, thus its details will not be discussed here, but early results can be found in the literature[30]. The awareness of the optimal potential distributions turns such a system into a smart-system since, through real-time monitoring of the blade vibrations, it is possible to automatically maximise its efficiency and minimise the blade stress whenever resonance occurs.

In the following sections, the analytical model of the optimal voltage distribution on rotating turbomachinery blades will be presented (Section 2). The kinematics of twisted blades and the inertial loads of rotating blades are derived in theAppendices A and B. In Section 3, the proposed method is applied to the case of an axial fan stage coupled with a strut front frame. At first, the possible resonance conditions for the proposed fan stage configuration are analysed (3.1), then the aerodynamic loads are determined under resonance conditions using CFD simulations (3.2). Finally, the aerodynamic loads are used in the FEA simulations to numerically verify the optimal potential distribution provided by the analytical model. The findings are presented and discussed in Section 4.

2. Mathematical model for optimal electric potential distribution on PZT pairs in rotating turbomachinery blades

Typically, blade vibrations are damped by passive systems [31–33]. Nevertheless, the recent developments in smart materials have led researchers to study their possible application in multiple fields. Among these materials, PZTs appear to be particularly promising because of their high frequency response, large bandwidth and high resolution. They can be used in both active and passive systems, the first being more efficient but cumbersome to implement. However, although there are many studies on damping flexural [34–36] and torsional [37] vibrations of beams, there is a lack literature regarding real turbomachinery blades and even fewer papers related to the optimal positioning of PZT actuators. Notably, the position strongly influences their effectiveness. Numerous studies have been conducted regarding the optimal placement to damp a single mode [26, 38–40] or multimode in a beam. In [28], a new method has been proposed where the focus of the research was shifted from the research of the optimal placement to the concept of the optimal potential distribution and a more efficient system is obtained. All the PZT plates, which cover the entire beam, will always work to damp the vibrations, but the electric potential has to change its distribution according to the mode, or combination of modes, that must be damped. In this paper, the procedure will be extended to the case of actual turbomachinery blades. However, the differences concerning the previously proposed model are significant from both physical and methodological point of views. In [28], only the flexural problem of a simple non rotating cantilever beam with a constant rectangular cross-section was considered. In the current case, a rotating blade of an axial compressor with a non-symmetrical section varying along the radius has been studied. For such structures additional difficulties arise due to their complex geometry and the presence of inertial loads, caused by rotation, which was not taken into account in the previous work. Here, it is not possible to study only the flexural problem decoupled from the other deformations since the flexural ones are coupled with both the torsional and extensional parts. Bending and torsion are coupled since the shear centre and the centroid does not coincide, while the inertial loads associated with the blade rotation, induce the coupling of flexural and extensional deformations. In addition, the nonlinear part of the deformations must be considered to properly account for the contribution of the centrifugal actions on the eigenfrequencies. However, in this paper such couplings were exploited to reduce the entire vibrational field through the bending moment applied by the PZT actuators. Here, the PZTs are considered because they are capable of generating high bending moments which is due to their high d_{31} coefficient, as highlighted in the previous work.

By applying the principle of the virtual works, denoting the virtual works of the elastic, inertial, aerodynamic and piezoelectric forces as δL_e, δL_{in}, δL_a, and δL_p, respectively, the equilibrium equations can be written as:

$$\delta L_e = \delta L_{in} + \delta L_p + \delta L_a \tag{1}$$

If M_η, M_ζ and M_x are the internal elastic moments with respect to the axes η, ζ, ξ and $\chi_\eta, \chi_\zeta, \chi_\xi$ the relative curvatures, then the expression of δL_e will be [1] :

$$\delta L_e = \int_0^L \Big(M_\eta \, \widetilde{\chi}_\eta + M_\zeta \, \widetilde{\chi}_\zeta + M_x \, \widetilde{\chi}_x \Big) \mathrm{d}x \tag{2}$$

For δL_{in}, denoting the resultant of inertial forces with p_x^{in} p_η^{in} and p_ζ^{in} and the resultant moments for a unit length with q_x^{in} q_η^{in} and q_ζ^{in}, it is equal to [2]:

$$\delta L_{in} = \int_0^L \Big(p_x^{in} \, \widetilde{u} + p_\eta^{in} \, \widetilde{\alpha} + p_\zeta^{in} \, \widetilde{\gamma} + q_x^{in} \, \widetilde{\theta}_x + q_\eta^{in} \, \widetilde{\theta}_\eta + q_\zeta^{in} \, \widetilde{\theta}_\zeta \Big) \mathrm{d}x \tag{3}$$

where $\widetilde{\alpha}, \widetilde{\gamma}$ are the virtual displacements of the elasic centre in the η, ζ di-

[1]Details of the calculation are given in the Appendix A. The virtual quantities will be identified with a tilde.

[2]Details of the calculation are given in the Appendix B

rections. Finally the virtual work of the aerodynamic loads δL_a can be written as follows: [3]:

$$\delta L_a = \int_0^L (p_a \, \tilde{\gamma} + q_a \, \tilde{\theta}_x) \mathrm{d}x \tag{4}$$

The expression of the pressure acting on the blade surfaces due to the aerodynamic loads $P_a(t)$, which is required for the calculus of the aerodynamic pressure resultant $p_a(t)$, will be derived in Section 3.2. Here the focus is on the calculation of δL_p and the concept of the optimal potential distribution. The characteristics of the so-called Pin-Force model can be summarised as follows: if opposite electric potentials are applied to two PZT plates, they will deform in the opposite way. For example, considering the distribution depicted in Fig. 1 the upper plate will stretch outward while the bottom plate will constrict inward.

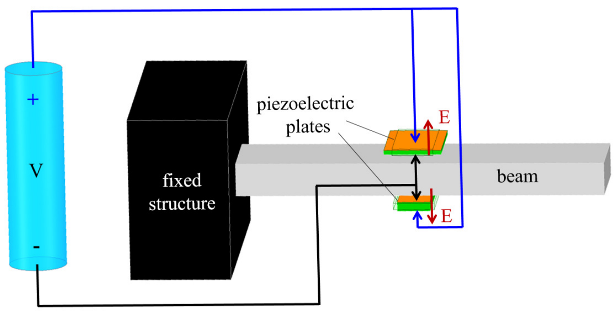

Figure 1: Potential distribution on a symmetrically placed PZT pair.

By blocking such deformations, i.e., gluing the plates on the beam in a symmetrical position (Fig. 2), PZT internal stresses will appear and they will be transferred to the beam via the interface.

[3] Details of the calculation are given in the Appendix C

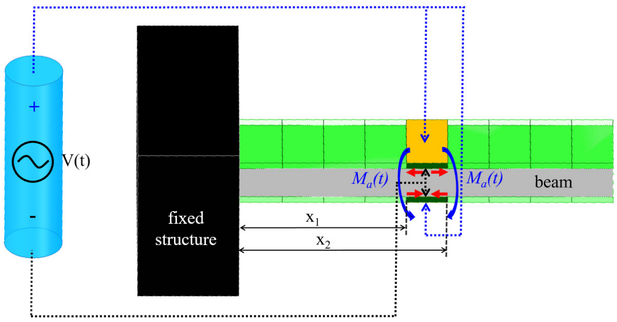

Figure 2: Actions of PPs glued on a beam.

In ([26]) it has been demonstrated that these interface stresses are concentrated at the edges of the piezoelectric plates and their action is analogous to that of two opposite flexural moments $M_a(t)$ concentrated at their extremities (Fig. 2) which induce beam vibrations. If the vibrations induced by $M_a(t)$ are modulated in counterphase with respect to those induced by the external load a damping effect is obtained.

Generally, the most dangerous vibrations occur when one or more eigenmodes are excited. Nevertheless, Nevertheless, the typical adopted airfoils for turbomachinery blades are designed with the aim of achieving the intended pressure profile, hence they exhibit asymmetric geometries. This entails the non-coincidence among the elastic and mass centroid axes for turbomachinery blades. Thereby, the excited modes are not purely torsional or flexural, but there is a coupling between bending and torsion. In this work this coupling will be exploited to damp the flexural-torsional vibrations by using the bending actions $M_a(t)$. It should be noted that M_a acts around the η-axis (Fig. 3) and, consequently, its virtual work is $M_a\,\overset{\sim}{\theta}_\eta$.

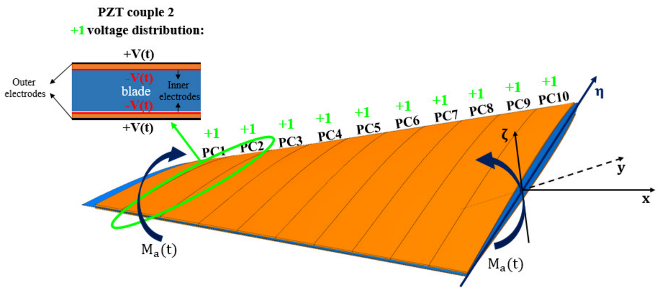

Figure 3: PZT actuators M_a on a blade.

If the blade vibrates according to the generic i-th eigenmode, then the virtual work of the piezoelectric forces can be written as:

$$\delta L_p^{(1)} = M_a \left(\widetilde{\theta_\eta^i} \,|_{\xi=\xi_2} - \widetilde{\theta_\eta^i} \,|_{\xi=\xi_1} \right) \tag{5}$$

where $M_a(t)$ is ([26]):

$$M_a(t) = \frac{\psi}{6+\psi} E_a b t_a t_b \Lambda(t) \tag{6}$$

and

$$\begin{cases} \psi = \frac{E_b t_b}{E_a t_a} \\ \Lambda(t) = \frac{d_{31}}{t_a} V(t) \end{cases} \tag{7}$$

The superscript $^{(1)}$ in Eq. 5 denotes the maximum piezoelectric work when the PZT actuators pairs are supplied with a single voltage distribution, i.e. with no voltage sign change, between ξ_1 and ξ_2. Under the same voltage V(t) (that is, the same value of $M_a(t)$) the virtual works δL_p will be higher, so the action of the PZT plates will be more efficient when the difference $\left(\widetilde{\theta_\eta^i} \,|_{\xi=\xi_2} - \theta_\eta^i|_{\xi=\xi_1} \right)$ is higher. Considering, for example, the optimal single voltage distributions for the first three modes (Figures 4(a) - 6(a)) , the quantity $\left(\widetilde{\theta_\eta^i} \,|_{\xi=\xi_2} - \widetilde{\theta_\eta^i} \,|_{\xi=\xi_1} \right)$ will assume its maximum value for $\xi_1 = \xi_1^*$ and $\xi_2 = \xi_2^*$. Thus, the PZT plates between ξ_1^* and ξ_2^* should be activated, while those between 0 and ξ_1^* should be deactivated. The corresponding optimal single voltage distributions for the second and third modes have been reported in Figures 4(b) - 6(b).

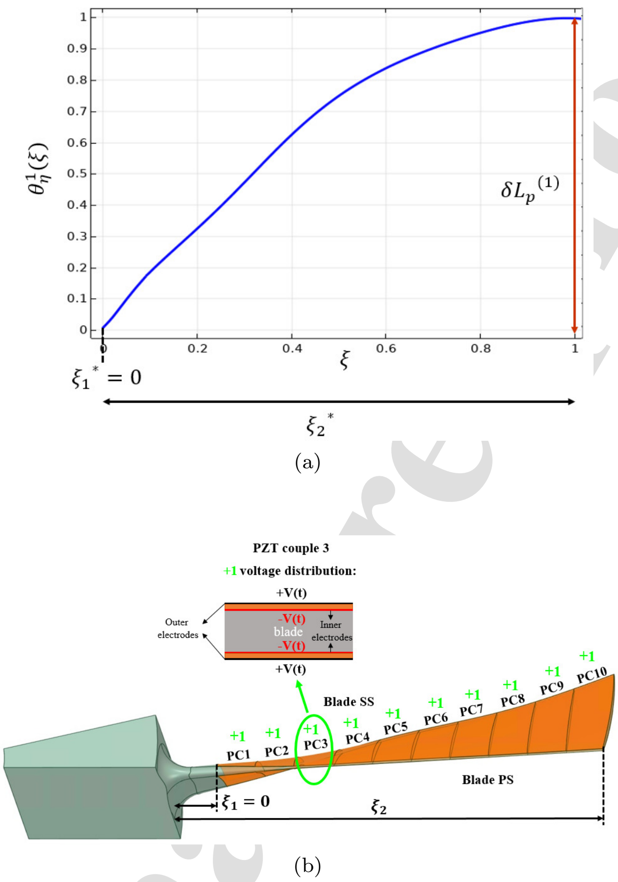

Figure 4: Example of PZT potential distribution: (a) the first prevalently flexural eigenmode of the blade, and (b) the optimal potential distribution when not all the PPs are activated. (PC = PZT couple)

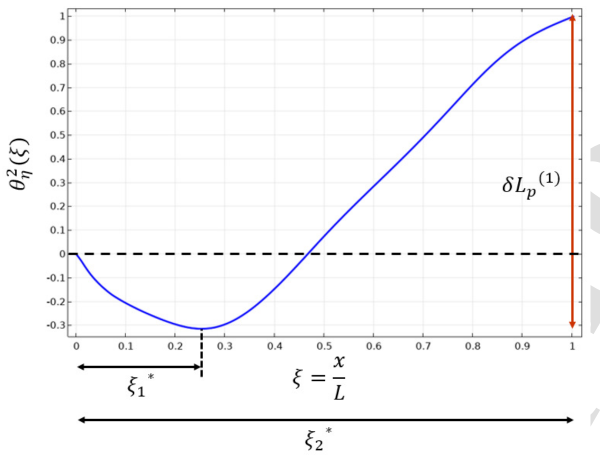

(a)

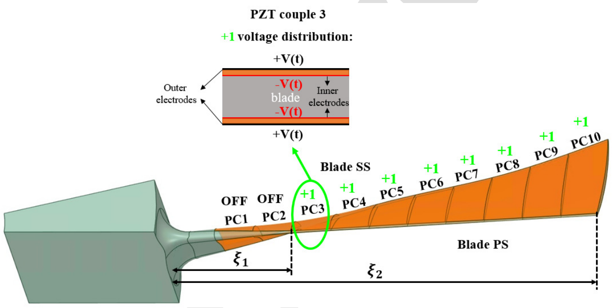

(b)

Figure 5: Example of PZT potential distribution: (a) the second prevalently flexural eigenmode of the blade, and (b) the optimal potential distribution when not all the PPs are activated. (PC = PZT couple)

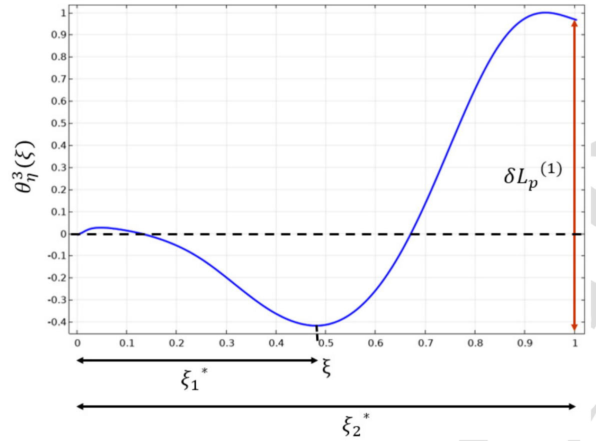

(a)

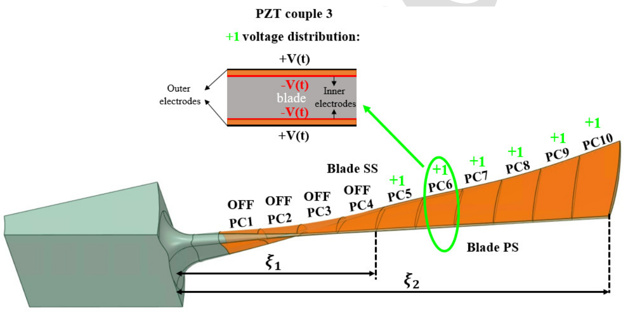

(b)

Figure 6: Example of PZT potential distribution: (a) the third prevalently flexural eigenmode of the blade , and (b) the optimal potential distribution when not all the PPs are activated. (PC = PZT couple)

However the system can reach a higher efficiency activating all the piezoelectric plates (also those between 0 and ξ_1^*) by switching the sign of the voltage distribution in ξ_1^*, in fact in this case the virtual works of the piezoelectric forces will be (Figures 7(a) - 8(a)):

$$\begin{aligned}\delta L_p^{(2)} &= M_a \Big[\Big(\overset{\sim}{\theta_\eta^i} \,|_{\xi=\xi_2^*} - \overset{\sim}{\theta_\eta^i} \,|_{\xi=\xi_1^*} \Big) - \Big(\overset{\sim}{\theta_\eta^i} \,|_{\xi=\xi_1^*} - \overset{\sim}{\theta_\eta^i} \,|_{\xi=0} \Big) \Big] = \\ &= M_a \Big(\overset{\sim}{\theta_\eta^i} \,|_{\xi=\xi_2^*} - 2\, \overset{\sim}{\theta_\eta^i} \,|_{\xi=\xi_1^*} \Big) = \delta L_p^{(1)} + \delta L_p^* > \delta L_p^{(1)} \end{aligned} \tag{8}$$

where the superscript $^{(2)}$ denotes the maximum piezoelectric work when the PZT actuators pairs are supplied with a dual voltage distribution, i.e. the voltage distribution between 0 and $\xi_1 = \xi_1^*$ has the opposite sign of the voltage distribution between $\xi_1 = \xi_1^*$ and $\xi_2 = \xi_2^*$. (PC = PZT couple)

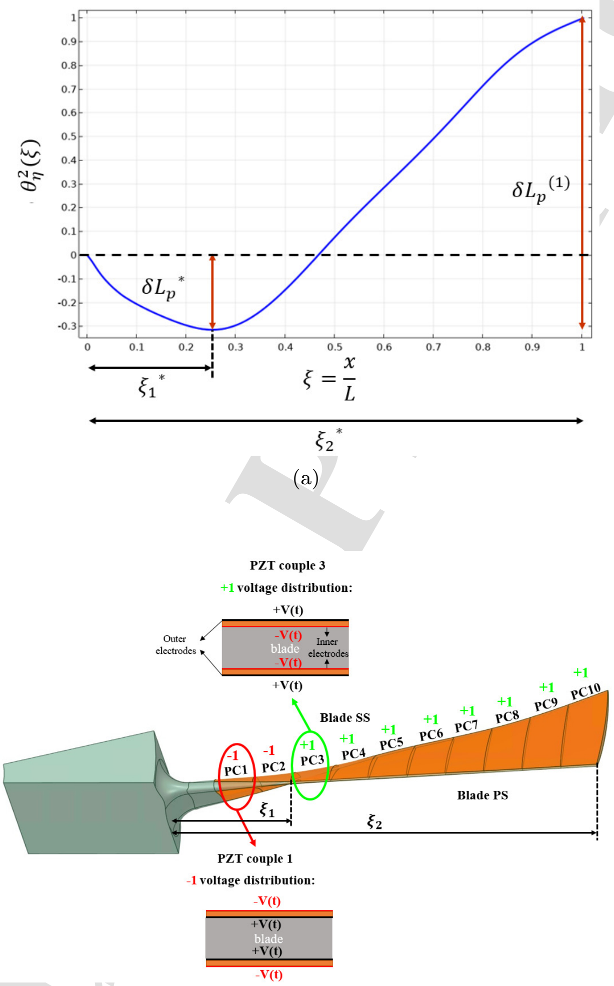

Figure 7: Example of PZT potential distribution: (a) the second prevalently flexural eigenmode of the blade, and (b) the optimal potential distribution with the activation of all the PPs. +1 and −1 potential distributions are 180° phase-shifted. (PC = PZT couple)

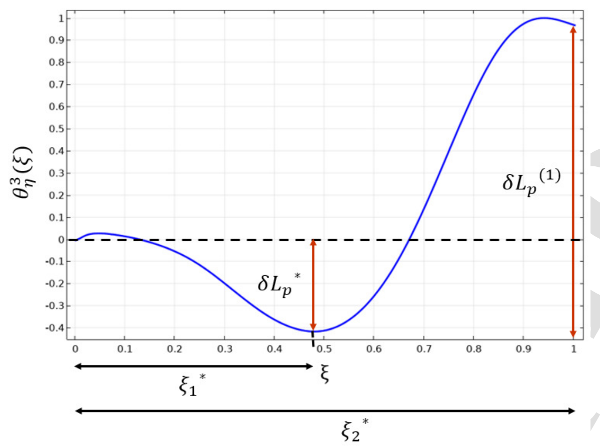

(a)

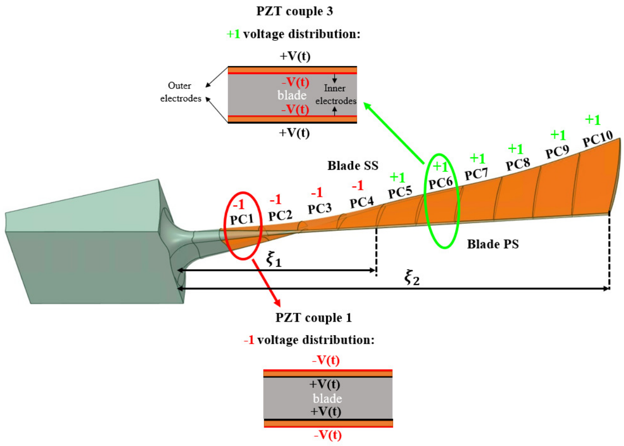

(b)

Figure 8: Example of PZT potential distribution: (a) the third prevalently flexural eigenmode of the blade, and (b) the optimal potential distribution with the activation of all the PPs. +1 and −1 potential distributions are 180° phase-shifted. (PC = PZT couple)

The corresponding potential distribution has been reported in Figures 7(b) 8(b). Generalising the procedure: changing the sign of the electric potential at every point where $\theta_\eta^i(\xi)$ shows a minimum or a maximum [28], every eigenmode $\theta_\eta^i(\xi)$ can be damped with all the PZT plates activated at all times to maximize the system efficiency. In section **4**, the proposed model is implemented and different electrical potential distributions are tested and their results are compared with each other.

3. Case study: axial fan stage coupled with a strut front frame

The proposed method is applied to an axial fan stage composed of 24 rotor blades coupled with a three-strut front frame. The fan blade was designed based on some available geometric and material data from an actual fan [41] (Table 1 and Fig. 9.

Table 1: Fan blade design parameters [41] .

Nominal shaft speed	3,000 rpm
Tip radius	1.00 m
Axial chord	0.09 m (hub), 0.11 m (tip)
Blade height	0.65 m
Twist	Free-vortex flow
Number of blades	24
Airfoil profiles	NACA series (radially varying from 0018 to 0004)
Material	Ti-Al-6V
Density [kg/m^3]	4,500
Young's modulus [GPa]	110
Poisson's Ratio	0.33
Yield Strength [MPa]	880
Fatigue Strength [MPa]	410

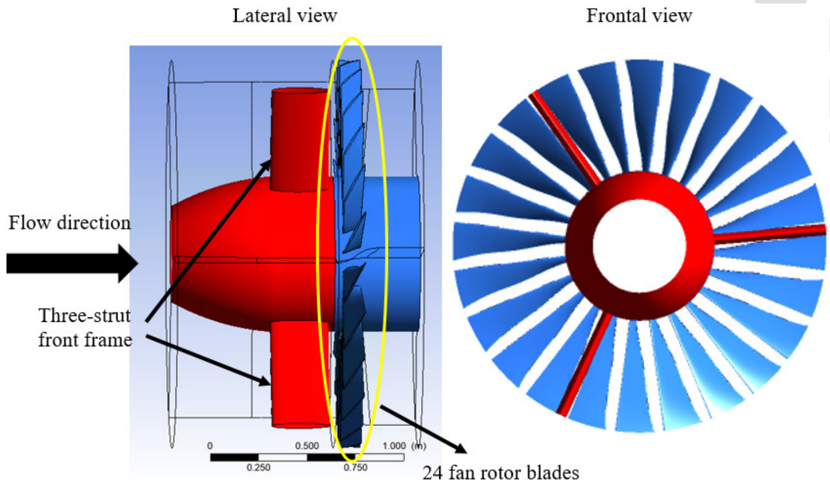

Figure 9: Axial fan stage configuration.

The presence of the upstream struts induces stationary inlet flow distortions that generate aerodynamic loads at low engine orders which may excite the lower eigenmodes of the blades and affect the downstream fan performance. In what follows, the resonance conditions of the fan stage under study are ascertained. Such analysis has been performed by means of FEA in Section 3.1. Thereafter, CFD analysis is performed to evaluate the aerodynamic loads, i.e., the term $p_a(t)$ in Eq. 4, acting on the blades under the previously identified resonance conditions (Section 3.2). Once the aerodynamic loads have been obtained, FEA analysis is carried out again to evaluate the stress induced on the blades under resonant conditions and to identify the best potential distribution (BPD), which has to be provided to the PPs to achieve the maximum stress mitigation (Section 4).

3.1. FEA: resonance conditions analysis

The FEA performed for both the identification of the possible resonance conditions and blade stress evaluation at resonance was conducted by exploiting the cyclic symmetry condition, which reduced the model complexity and computing costs, without jeopardising the solution accuracy ([42], [43]).

Thereby, the blisk dynamics can be analysed by considering a single sector (i.e., the fundamental sector) and subsequently replicating it N times (24 in the present case) so the full disc solution can be obtained. The eigenmodes of cyclically symmetric structures are associated with a harmonic index, referred to as the nodal diameter (ND). Fig. 10(b) shows a generic fundamental sector whereby the degrees of freedom associated with the corresponding nodes belonging to the lower ($\boldsymbol{u_A}$) and upper ($\boldsymbol{u_B}$) interface surfaces are related by the following equation:

$$\boldsymbol{u_B} = \mathrm{e}^{\mathrm{i}\phi} \cdot \boldsymbol{u_A} \tag{9}$$

where $\phi = k\phi_{fs} = k\frac{2\pi}{N}$ is the interphase blade angle, ϕ_{fs} is the angle between the lower and upper interface surfaces and $0 \leq k \leq \frac{N}{2}$ is the ND ($0 \leq k \leq \frac{N}{2} - 1$ if N is odd). The fixed boundary condition is represented by the nodes $\boldsymbol{u_F}$ reported in Fig. 10(b).

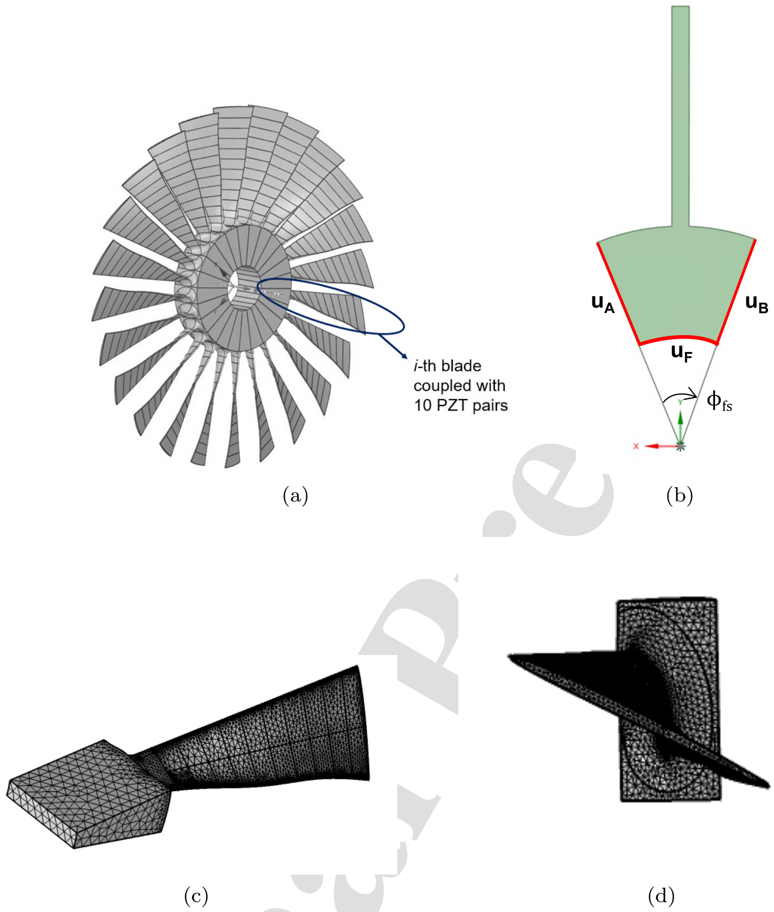

Figure 10: Fan rotor blisk: (a) fan blisk with arrays of PZT actuators mounted on each blade, (b) the generic fundamental sector, cyclic symmetry boundaries ($\boldsymbol{u_A}$ and $\boldsymbol{u_B}$) and fixed boundary ($\boldsymbol{u_F}$). Generated mesh on the fundamental sector: (c) first view, and (d) second view.

Unstructured tetrahedral elements were used to mesh the fan fundamental sector, which consists of approximately 52,000 elements (Fig. 10c-d). In Fig. 11 the first five modes of the fan blades are illustrated.

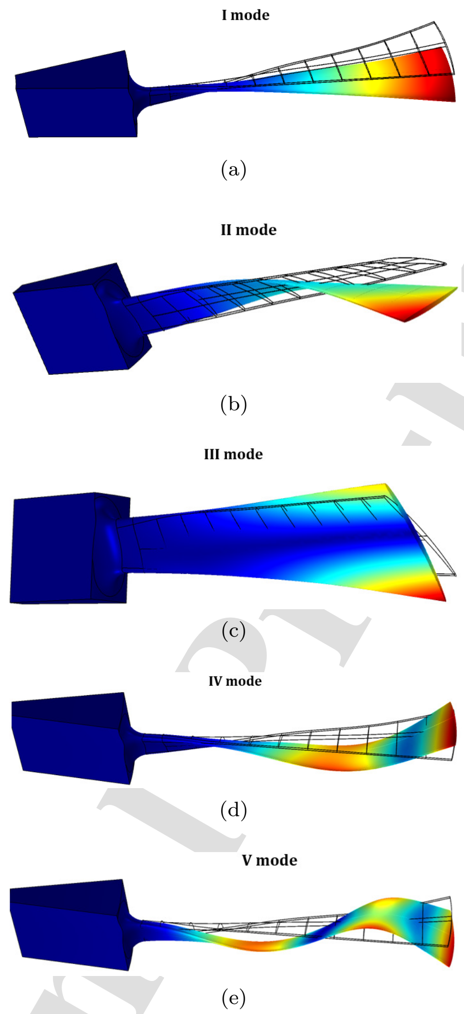

Figure 11: Lower blade modes: (a) I mode, (b) II mode, (c) III mode, (d) IV mode, (e) V mode

The first, fourth and fifth modes are similar to the first, second and third predominantly flexural blade eigenmodes, whereas the third mode represents the first predominantly torsional eigenmode. The second mode appears to be a combination of the second flexural and first torsional blade modes with a more pronounced flexural characteristic. The analysis of the possible resonant conditions of the blisk, within its operative speed range, was carried out by elaborating the SAFE diagram for the blisk [44–46]. Here, both the aerodynamic loads and eigenmodes are expressed as functions of the ND. The resonance condition is found when the frequency of the blisk eigenmode matches the frequency of the speed line at an integer value of the ND. In these cases, the aerodynamic forcing and the specific blisk eigenmode interact in the most detrimental way. For the present case study, 3EO and 6EO are relevant since a three-strut front frame is coupled with the fan stage. In Fig. 12 the interference diagram is reported at 2535 rpm because it is the speed that may lead to the resonance of the lower blades modes within the operating speed of the fan (60 - 100% of the nominal speed). Upon a closer inspection of the diagram, it can be seen that 3EO and 6EO disturbances may respectively excite the II blisk eigenmode characterised by three NDs (i.e., ND=3) (Fig. 13a, b) and the IV eigenmode (ND=6) (Fig. 13c, d).

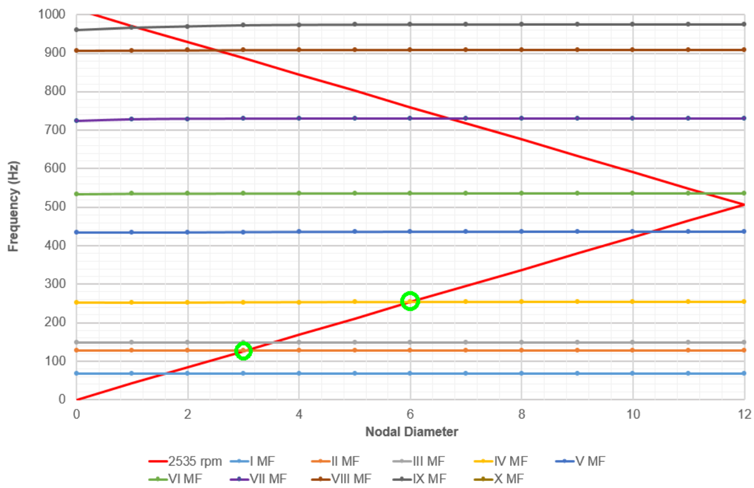

Figure 12: Blisk SAFE interference diagram. The 2535 rpm line and the first ten modal families (m.f.) are represented. The investigated crossing points are depicted in green.

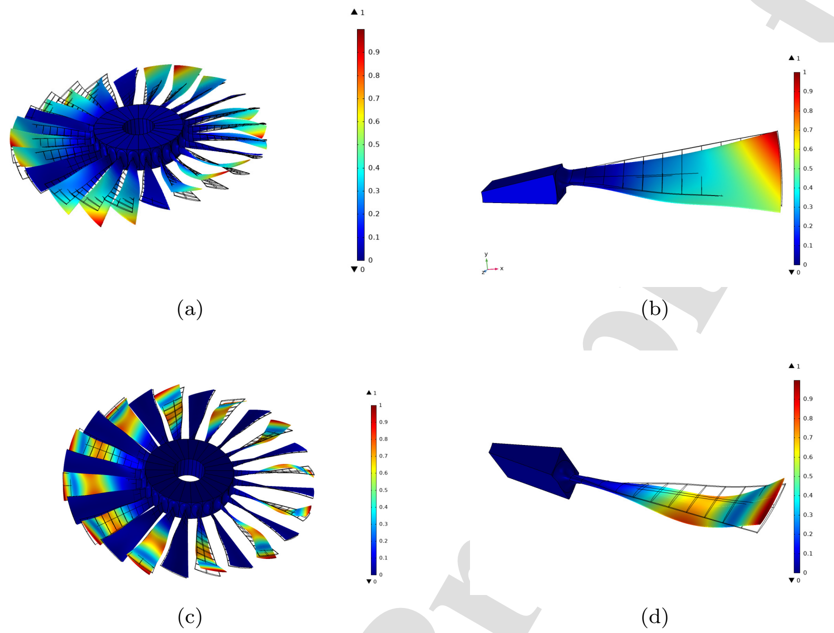

Figure 13: Considered fan blisk modes: (a) II mode ND=3 (full blisk), (b) II mode ND=3 (single sector), (c) IV mode ND=6 (full blisk), and (d) IV mode ND=6 (single sector).

3.2. CFD simulations: aerodynamic loads assessment

The commercial CFD software ANSYS CFX R19.2 was used to simulate both the steady and unsteady flows in the axial fan stage. The Reynolds-Averaged Navier-Stokes equations were discretised using a finite volume algorithm [47, 48]. Both the steady and unsteady studies were carried out by considering the shear stress transport turbulence model [49]. The interfaces between the stator and rotor were set as a mixing plane in the steady simulations and transient rotor-stator in the unsteady analysis. To predict transient phenomena such as vortex shedding, at reasonable computational cost, transient blade row methods were implemented in the CFX solver to solve the transient flow conditions with lower blade passages, instead of simulating the full-annulus. Among these, the time transformation (TT) is one of the most accurate methods in terms of predicting unsteady flows and performance data in turbomachinery. The flow across the interface of two contiguous blade rows can be obtained without introducing frequency errors which are then involved in other methods, such as profile transformation [50–53]. The TT method can be applied to compressible flows if the pitch ratio $S = \frac{S_{rb_1}}{S_{rb_2}}$ is $0.6 \leq S \leq 1.5$, where $S_{rb_1} = \frac{2\pi}{N_{rb_1}}, S_{rb_2} = \frac{2\pi}{N_{rb_2}}$ and N_{rb_1}, N_{rb_2} are the blades in the first and second blade rows. In the present case 24 rotor blades and three struts are involved and thus $S = 1$ ($S_{rb_1} = \frac{2\pi}{3}$, $S_{rb_2} = \frac{2\pi \cdot 8}{24}$). Therefore, 1/3 of the full-annulus is simulated in the present study. The fluid conditions are listed in Table (2).

Table 2: Fluid conditions.

Pressure ratio	1.2
Absolute inlet velocity	150 m/s (purely axial)
Fluid	Ideal gas (Air at 288 K)
Mach at the tip	1.0

The pressure and suction sides of the fan blade were thickened by 0.4 mm to include the PZT actuator footprint. The axial gap between the trailing edge (TE) of the struts and the leading edge (LE) of the rotor blades was set to 70 mm. The struts profiles were based on NACA 0026. The computing grids were generated using the ATM optimised topology feature available in ANSYS Turbogrid. The mesh of the computational domain consists of 348,500 elements (366,600 nodes) for the fan and 442,200 elements (469,000 nodes) for the strut. A mesh convergence analysis was carried out to identify the most efficient mesh Fig.14. The details for the three adopted meshes are listed in Table 3. The grids were densified by prioritising the areas near the blades.

Table 3: Details of the three meshes considered for the grid influence study.

	Fan domain	
Mesh	**Total number of elements**	**Total number of nodes**
Coarse	168.5k	179.7k
Medium	348.5k	366.6k
Fine	622.8k	649.7k
	Strut domain	
Mesh	**Total number of elements**	**Total number of nodes**
Coarse	185.1k	199.5k
Medium	442.2k	469.0k
Fine	915.0k	953.7k

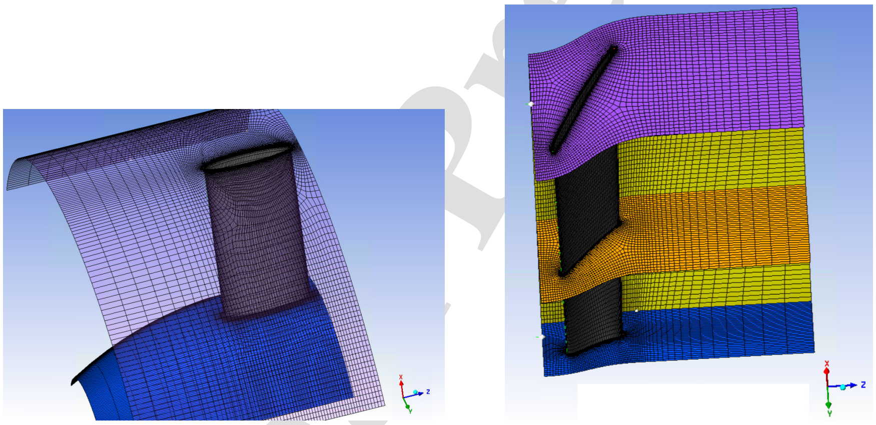

(a) (b)

Figure 14: (a) Strut and (b) rotor computational grid for the medium mesh.

Total pressure, total temperature and the inlet flow angle were set as the inlet boundary conditions in steady-state simulations, while the average static pressure was specified at the outlet. All the boundary conditions are listed in Table 4. The fan speed and the convergence criteria for the root mean square (RMS) residuals were set at 2535 rpm and $5 \cdot 10^{-5}$ for all the steady-state simulations.

Table 4: Steady-state simulation inlet and outlet boundary conditions at 2535 rpm.

Inlet	
$\mathbf{P}_{total}$	111,168 kPa
$\mathbf{T}_{total}$	296 K
Flow direction	purely axial
Outlet	
$\mathbf{P}_{static}$ average	113,135 kPa

Table 5: Comparison of the mass flow rate, total pressure ratio and isentropic efficiency obtained for the three different meshes.

	Coarse	**Medium**	**Fine**
Mass flow [kg/s]	379.7	382.1	382.7
Total pressure ratio	1.109	1.110	1.110
Isentropic efficiency %	90.28	90.87	91.00

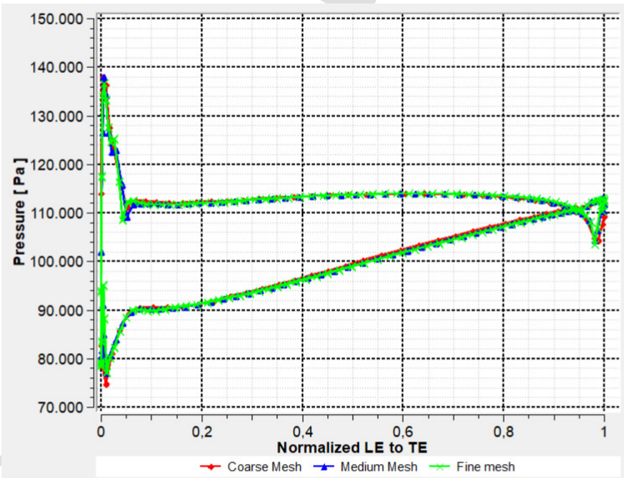

Figure 15: Fan blade loading chart calculated at the midspan. The normalised axial distance from the LE to the TE of the blade represents the abscissa of the plot.

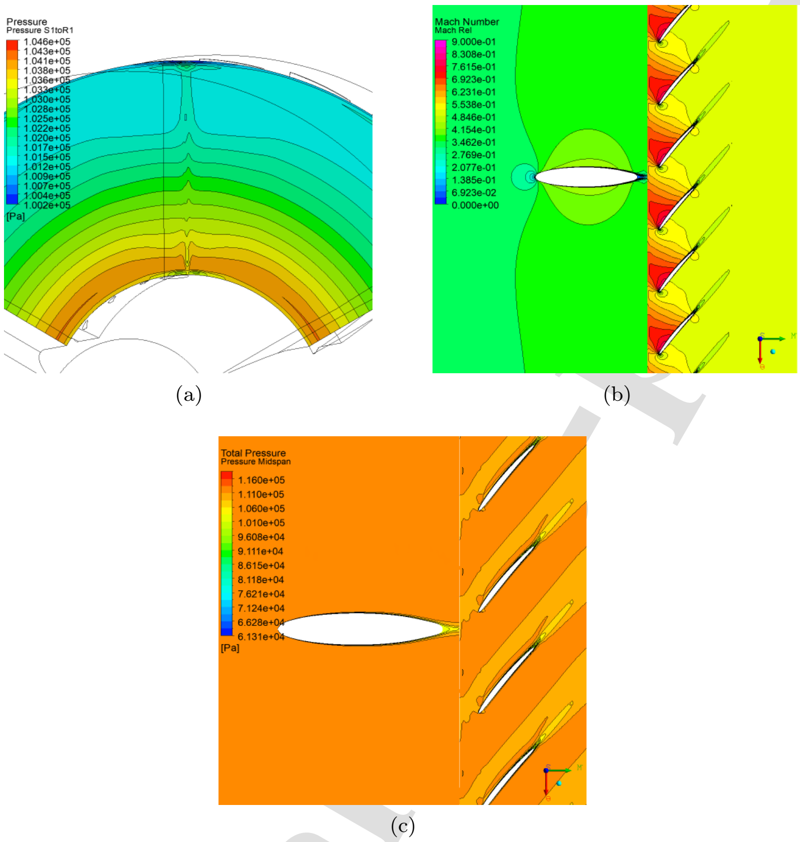

Figure 16: (a) Radial pressure distribution at the interface between strut and rotor, (b) relative Mach distribution and (c) total pressure distribution at midspan.

The calculated mass flow rate, total pressure ratio and isentropic efficiency hardly vary from coarse to fine mesh, as seen in Table 5. In Fig. 15 is reported the fan blade loading chart obtained with the different meshes. The results calculated with the medium and finer mesh are similar. Thus the average mesh shows a good trade-off between accuracy and computational costs, and it was later considered in the unsteady simulations. The radial pressure distribution at the interface between the strut and fan blade domains, the relative Mach, as well as the total pressure distribution at the midspan, are reported in Fig. 16. The strut generates a marked flow distortion upstream the fan blades.

After analysing the average flow through the fan stage, it is possible to study the unsteady flow characteristics to calculate the pressure fluctuation over time using the unsteady CFD simulation. The initial conditions were derived from the steady-state analysis and the RMS residual target for the inner loops in the unsteady simulation was set to $5 \cdot 10^{-5}$. The variables (i.e., temperature, pressure, etc.) from the TT simulation were calculated and stored by the CFX solver using ten Fourier coefficients. Then the pressure $P_a(t)$ acting on the blade surfaces is represented as:

$$P_a(t) = A_0 + \sum_{k=1}^{NFC} \left(A_k \cos(k\omega t) + B_k \sin(k\omega t)\right) \tag{10}$$

where A_0 is the real time-averaged value, k is the index of the mode, ω is the rotation frequency of the blisk, NFC is the total number of modes used to reconstruct the variable and A_k and B_k are real coefficients. The rotor passing period ($9.87 \cdot 10^{-4}$s) was split into 15 time steps to accurately capture excitation frequencies up to 15,000 Hz. The simulation was run for two full shaft revolutions (48 periods) and the harmonic pressures acting on the fan blade, which depend on the coefficients (A_k, B_k), were then obtained. An example of the harmonic pressure distribution on the pressure and suction sides of the blades, related to the 3EO and 6EO forcing frequencies, is reported in Figures 18 – 19.

At this stage, all the coefficients (A_k, B_k) have been obtained via unsteady CFD simulation. Then, the virtual work of the aerodynamic loads δL_a (Eq. 4) can be determined since the resultant of the aerodynamic pressure $p_a(t)$ can be calculated as described in Appendix C.

4. Results and discussion

The blade forced response can be obtained by mapping the CFD harmonic pressure loads on the blade surfaces obtained in 3.2 and evaluating the pre-stressed frequency response analysis via FEA. In the first step, the stationary solution is calculated by applying the centrifugal load and the mean pressure distribution A_0 caused by the steady aerodynamic load (Fig. 20). Then, the blade response to the aerodynamic harmonic pressure load, which fluctuates around the static one, can be computed in subsequent analysis. In this study, only the second and fourth modes of the blisk can be excited by the aerodynamic loads associated with the 3EO and 6EO. Fig. 17 shows the fast fourier transform (FFT) of the pressure evaluated at the LE at 50% and 75% of the blade span. The FFT shows some meaningful harmonics (3EO, 6EO, 24EO and 48EO) but only 3EO and 6EO can excite lower blisk eigenmodes (Fig. 12). It follows that only the coefficients (A_3, B_3) and (A_6, B_6) have to be considered in the frequency response analysis (Figs. 18 - 19).

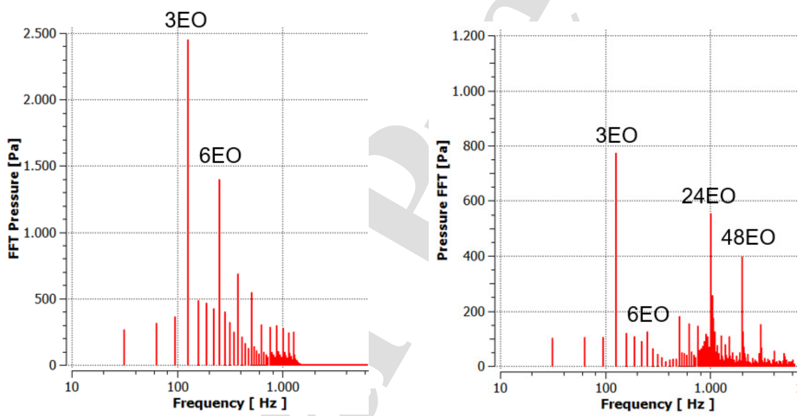

(a) (b)

Figure 17: Pressure FFT calculated at the leading edge of the fan blade at: (a) 50% of the span, and (b) 95% of the span.

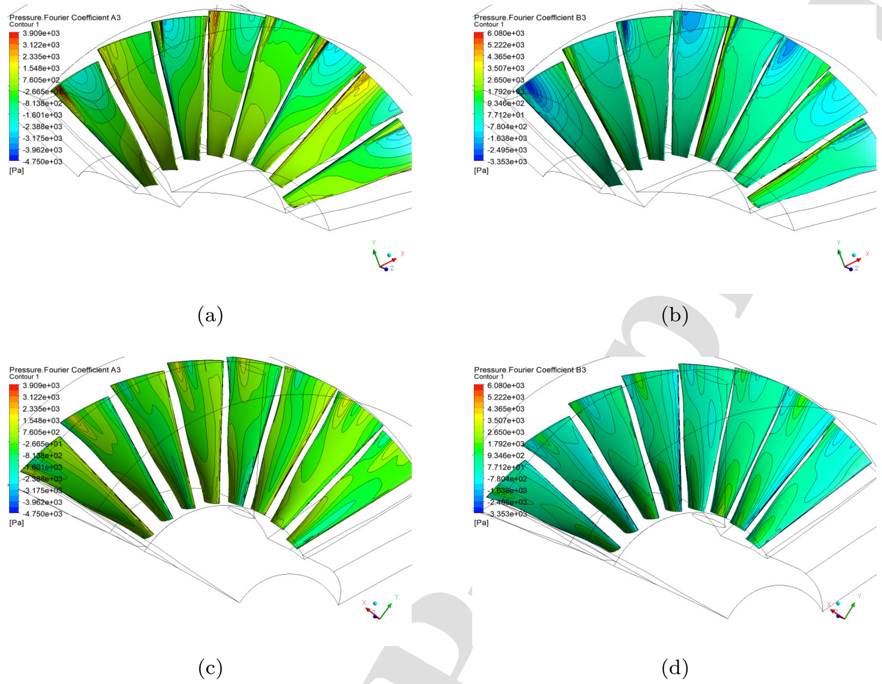

Figure 18: 3EO pressure distribution in terms of Fourier coefficients: (a) A_3 on the pressure side, (b) B_3 on the pressure side, (c) A_3 on the suction side, and (d) B_3 on the suction side.

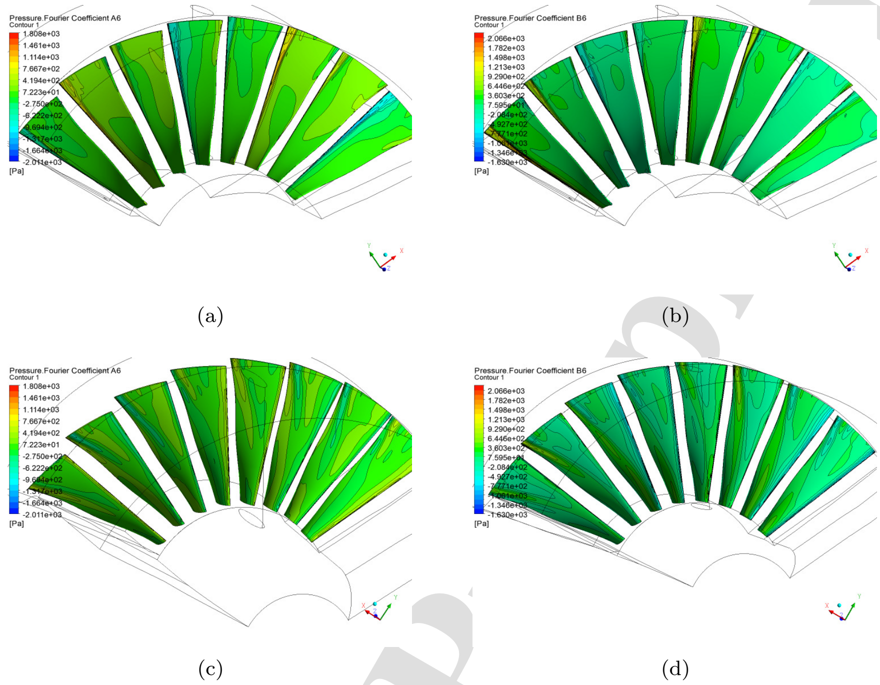

Figure 19: 6EO pressure distribution in terms of Fourier coefficients: (a) A_6 on the pressure side, (b) B_6 on the pressure side, (c) A_6 on the suction side, and (d) B_6 on the suction side.

The method proposed in Section 2 is applied to dampen the vibrations of the II and IV eigenmodes of the fan rotor blisk. Each blade is coupled with two arrays of PZT actuators fixed on both pressure and suction sides (Fig. 10a). As discussed in Section *2*, the electric potential applied to the inner and outer electrodes of each PZT couple must show the opposite sign (Fig. 21). The PZT actuators have been modeled considering the strain-charge constitutive equations and the material specifications are reported in Table (6). The blisk structural damping ratio was set to $\zeta = 0.002$, according to [21].

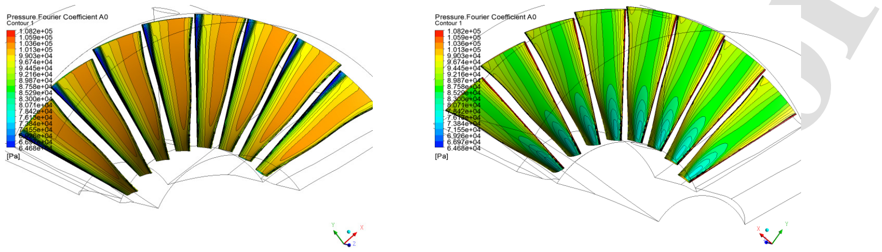

(a) (b)

Figure 20: Mean pressure component (A_0) distribution on the rotor blades for (a) the pressure side, and (b) suction side.

Table 6: PZTs material specifications.

	Piezoelectric actuators
Material	PZT-5H
Density [kg/m^3]	7,500
$\mathbf{d}_{31}$ [C/N]	-2.74$\cdot 10^{-10}$

Then, if ten PZT pairs are considered, $2^{10} = 1024$ possible voltage distributions (Table 7) can be explored to find the one that achieves the highest stress reduction. For example, the j-th potential distribution is depicted in Fig. 21.

Table 7: Possible voltage distributions for ten PPs.

PZT pair / Combinations	**1**	**2**	**3**	**4**	**5**	**6**	**7**	**8**	**9**	**10**
1	+1	+1	+1	+1	+1	+1	+1	+1	+1	+1
2	-1	+1	+1	+1	+1	+1	+1	+1	+1	+1
...	...	...	...	...	...	...	...	...	...	...
j	-1	+1	-1	-1	+1	+1	+1	+1	+1	-1
...	...	...	...	...	...	...	...	...	...	...
1024	-1	-1	-1	-1	-1	-1	-1	-1	-1	-1

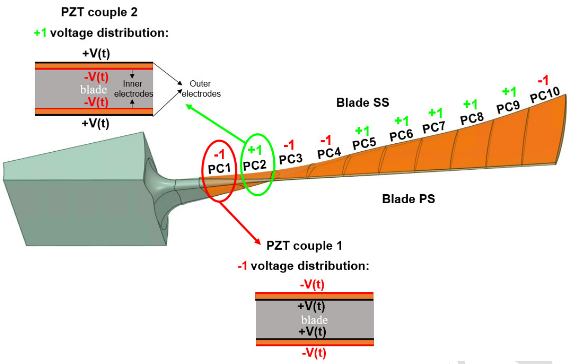

Figure 21: j-th potential distribution on the i-th blade from the blisk. The outer and inner electrodes of each PC must always be driven with opposite sign voltage. (PC = PZT couple)

However, for a j-th configuration there exists an antisymmetric i-th configuration (Table 8):

Table 8: Antisymmetric voltage distributions for ten PPs.

PZT pair / Combinations	**1**	**2**	**3**	**4**	**5**	**6**	**7**	**8**	**9**	**10**
...	...	...	...	...	...	...	...	...	...	...
j	-1	+1	-1	-1	+1	+1	+1	+1	+1	-1
...	...	...	...	...	...	...	...	...	...	...
i	+1	-1	+1	+1	-1	-1	-1	-1	-1	+1
...	...	...	...	...	...	...	...	...	...	...

Only one of them exerts the damping action while the other will act in-phase with the external load, resulting in excitation. Hence, in the following analysis, only the 512 damping configurations are considered.

In this paper, the focus is on their use to mitigate blade stress. The total von Mises stress is:

$$\sigma_{tot} = \sigma_m + \Delta\sigma_a \tag{11}$$

It consists of two components: (a) the mean (or static) stress σ_m caused by the centrifugal load and mean pressure load (Eq. 10) and (b) the alternating stress $\Delta\sigma_a$ caused by the harmonic loads. The total stress was first calculated for each aerodynamic load without activating the actuators to establish the reference stress level. In Fig. 22 the static and total von Mises stress have been reported considering only the 3EO aerodynamic load (II blisk eigenmode excitation) with deactivated PZTs, while Fig. 23 shows the analogous results in the case of 6EO forcing (IV blisk eigenmode excitation).

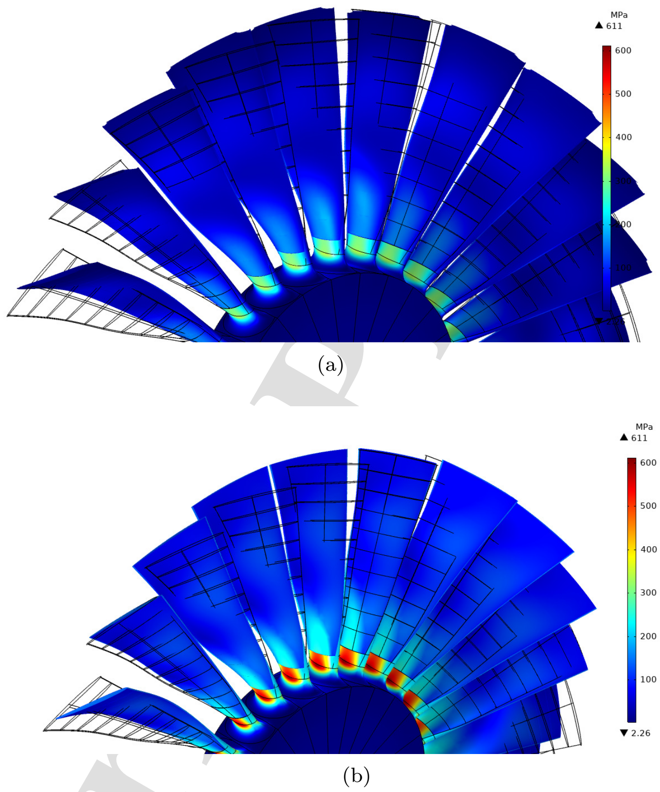

Figure 22: Total von Mises stress (MPa) calculated considering: (a) only the pre-load (centrifugal + mean aerodynamic load) (deactivated PZTs), and (b) the total load: pre-load and harmonic pressures at 3EO forcing frequency (deactivated PZTs).

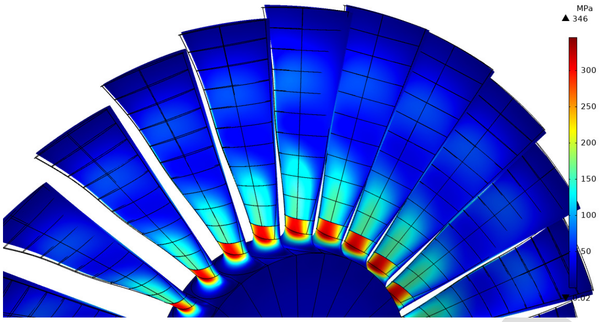

(a)

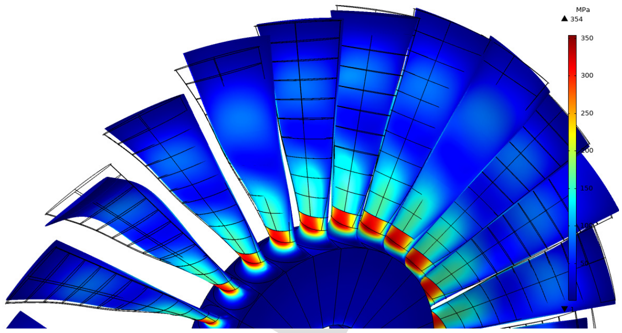

(b)

Figure 23: Total von Mises stress (MPa) calculated considering: (a) only the pre-load (centrifugal + mean aerodynamic load) (deactivated PZTs), and (b) the total load: pre-load and harmonic pressures at 6EO forcing frequency (deactivated PZTs).

The highest stress area is located at the suction side of the blade root. In this zone the mean stress caused by the centrifugal and mean pressure load is equal to $\sigma_m = 346$ MPa (Fig. 22(a) - 23(a)), while the amplitude of the alternating component of the stress $\Delta\sigma_a$ is approximately 265 MPa in the case of 3EO forcing (Fig. 22(b)). Moreover, $\Delta\sigma_a$ is approximately 10 MPa for the 6EO forcing case (Fig. 23(b)). It follows that $\Delta\sigma_a$ for the 6EO aerodynamic load is almost negligible since it is about 4% of the one induced by 3EO forcing; hence, the mitigation of $\Delta\sigma_a$ when the II mode of the blades is excited will be addressed first.

Once the reference stress level was assessed, the PZT action can be included in the frequency response study and all the 512 voltage distributions were simulated to compare the stress mitigation performances. The BPD was considered as the one that minimises the alternating stress component ($\Delta\sigma_a$) acting on the blades for each EO forcing, as it is the most detrimental factor from the fatigue standpoint.

For 3EO forcing, all the 512 results have been reported in Fig. 24.

The distributions have been rearranged from best to worst so that the first configuration coincides with the BPD, as illustrated in Figure 25. Further analysis of the Fig. 24 reveals the robustness of the proposed strategy. There are 16 potential distributions for which 62 – 73% stress reduction can be achieved (73% can be obtained for the BPD II, Table 10). The distributions closest to BPD II may show the potential sign change of one or two PPs located immediately before or after the PP whereby the optimal potential sign switch is expected. As a result, even if a non-optimal potential distribution is activated, the small reduction of damping efficiency is acceptable.

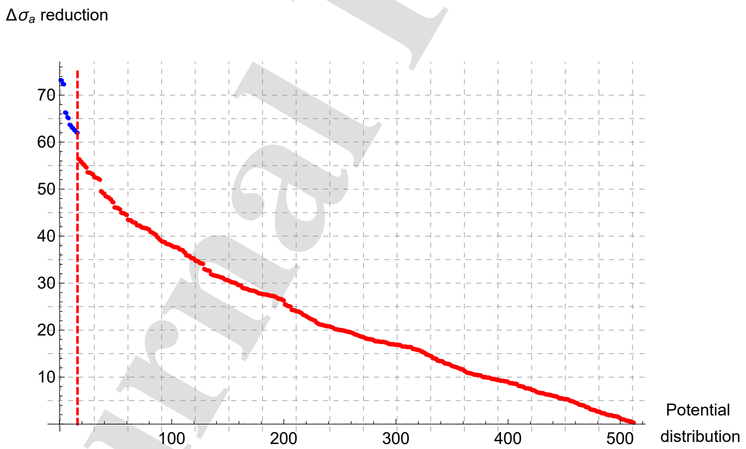

Figure 24: 3EO forcing: $\Delta\sigma_a$ percentage reduction reported for all the possible PZT potential distributions. The maximum reduction $\Delta\sigma_a^{max}$ can be obtained for the BPD II. The data are rearranged in descending order. Blue points denote the potential distributions for which 62 - 73% stress reduction can be achieved, red points denote the potential distributions for which the stress reduction is lower than 62%.

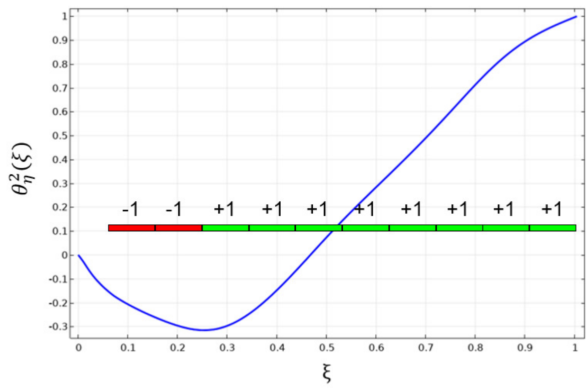

Figure 25: $\theta_\eta^2(\xi)$ for the II blisk mode (ND=3) and BPD

425 The results appear to be consistent with the theoretical model predictions. From Fig. 25, the potential switches its sign (from -1 to $+1$) at the local minimum of $\theta_\eta^2(\xi)$. The activation of the piezoelectric plates reduces the value of $\Delta\sigma_a$ obtaining the maximum stress mitigation for the BPD II. The considered potential distributions A, B and BPD II are reported in Table 9, while the results
430 are summarised in Table 10:

Table 9: List of potential distributions considered for the illustrations of Figs. 26. (PP= piezoelectric pair)

Distribution	PP 1	PP 2	PP 3	PP 4	PP 5	PP 6	PP 7	PP 8	PP 9	PP 10
A	-1	+1	-1	+1	+1	-1	+1	+1	+1	-1
B	-1	+1	-1	+1	+1	+1	+1	+1	-1	+1
BPD II	-1	-1	+1	+1	+1	+1	+1	+1	+1	+1

Table 10: Comparison between mean and alternating stress obtained by activating different potential distributions for the same target eigenmode.

EO forcing	Excited mode	Potential distribution	Voltage amplitude [V]	σ_m [MPa]	$\Delta\sigma_a$ [MPa]	$\Delta\sigma_a$ reduction (%)
3EO	II, ND=3	–	0	346	265	–
3EO	II, ND=3	A	280	346	173	≈ 35%
3EO	II, ND=3	B	280	346	132	≈ 50%
3EO	II, ND=3	**BPD II**	280	346	72	≈ **73%**

To have a clearer interpretation of the results, the von Mises stress is reported in Fig. 26, taking into account the full load and de-activated PZTs, then the full load with the piezoelectric active damping for two generic distributions which achieve 70% (configuration A) and 50% (configuration B) of the maximum achievable stress reduction, and finally, showing the BPD.

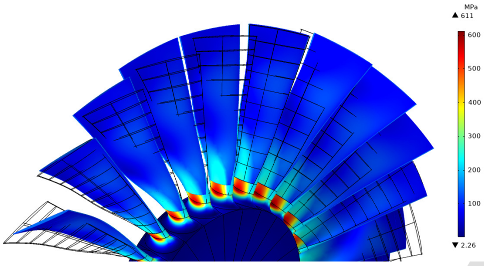

(a)

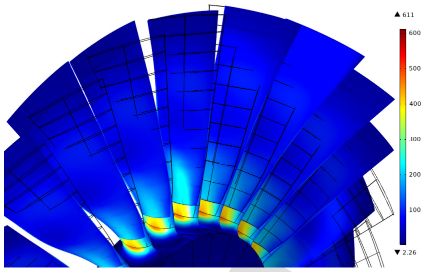

(b)

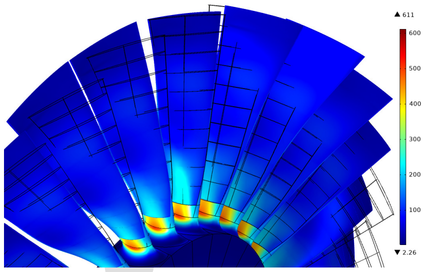

(c)

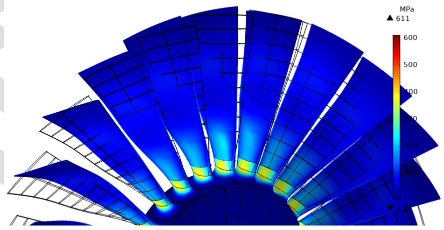

(d)

Figure 26: Total von Mises stress (MPa) calculated considering: (a) the total load: pre-load and harmonic pressures at 3EO forcing frequency (deactivated PZTs), (b) activation of the potential distribution A, (c) the potential distribution B and (d) the BPD II.

Although the 6EO forcing excites the IV mode but does not yield a dangerous alternating stress level, this may not be the case for other turbomachinery configurations. For example, if the number of struts in the front frame was six, most likely the alternating stress caused by 6EO forcing would be greater than that due to the 3EO forcing. The presence of six flow disturbances located upstream or downstream of the fan rotor will cause 6EO forcing on the rotor blades and if the shaft speed is 2535 rpm, then the IV blisk mode will be excited. To substantiate the proposed potential distribution method, the case of the IV mode resonance caused by 6EO forcing has also been analysed and the BPD has been verified.

Similar results with respect to the 3EO forcing case (Fig. 24) have been obtained for 6EO forcing Fig. 27.

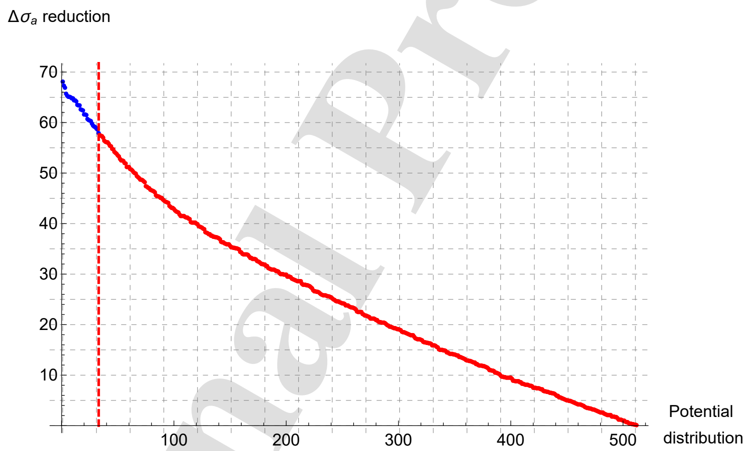

Figure 27: 6EO forcing: $\Delta\sigma_a$ percentage reduction reported for all the possible PZT potential distributions. The maximum reduction $\Delta\sigma_a^{max}$ can be obtained for the BPD IV. The data are rearranged in descending order. Blue points denote the potential distributions for which 58 - 68% stress reduction can be achieved, red points denote the potential distributions for which the stress reduction is lower than 58%.

In the case of 6EO forcing, there are 33 potential distributions for which 58 - 68% stress reduction can be achieved, thereby confirming the robustness of the proposed method and also for the IV eigenmode excitation.

The BPD is shown in Fig.28 where the potential sign switch occurs again in correspondence with the minimum of the mode shape $\theta_\eta^4(\xi)$.

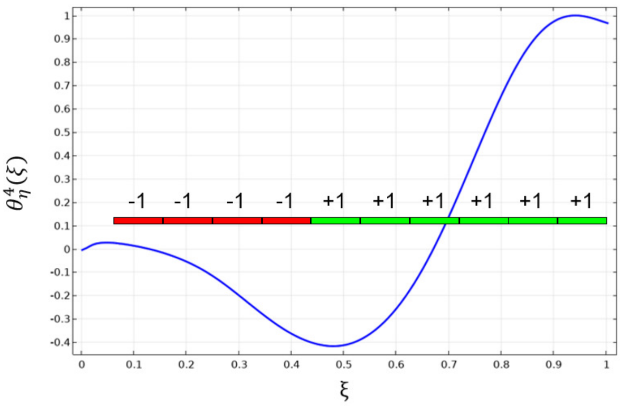

(a)

Figure 28: $\theta_\eta^4(\xi)$ for the IV blisk mode (ND=6) and BPD

The von Mises stress is reported in Fig. 29. The amplitude of the alternating component of the stress $\Delta\sigma_a$ is approximately 10 MPa since the static stress σ_m is 346 MPa (Fig. 29(a)). The activation of the PZT plates reduces the value of $\Delta\sigma_a$ obtaining the maximum stress mitigation in correspondence with the BPD IV (d). The results are summarised in Table 11, while the potential distributions C and D, which enables 0.75 and 0.5 of the maximum stress reduction (Fig. 29(b) and (c)), which is 68% for the BPD IV, are reported in Table 12.

Table 11: Comparison between mean and alternating stress obtained by activating different potential distributions for the same target eigenmode.

EO forcing	**Excited mode**	**Potential distribution**	**Voltage amplitude** [V]	σ_m [MPa]	$\Delta\sigma_a$ [MPa]	$\Delta\sigma_a$ **reduction (%)**
6EO	II, ND=6	–	0	346	10	–
6EO	IV, ND=6	C	41	346	6.6	$\approx$ 33%
6EO	IV, ND=6	D	41	346	4.4	$\approx$ 56%
6EO	IV, ND=6	**BPD IV**	41	346	3.2	$\approx$ **68%**

Finally, it was also observed the impact of the BPD II on the fourth mode or the BPD IV on the second mode. If the IV mode of the blisk is excited and the BPD II is activated, approximately 55% stress mitigation can be achieved. Conversely, if the II mode is excited and the BPD IV is activated, then 54%

Table 12: List of potential distributions considered for the illustrations of Figs. 29. (PP= piezoelectric pair)

Distribution	PP 1	PP 2	PP 3	PP 4	PP 5	PP 6	PP 7	PP 8	PP 9	PP 10
C	+1	+1	-1	-1	+1	-1	-1	-1	+1	-1
D	+1	-1	-1	+1	+1	-1	-1	-1	-1	-1
BPD IV	-1	-1	-1	-1	+1	+1	+1	+1	+1	+1

stress reduction is obtained. The different location of ξ_1^* in the BPD II and BPD IV induces a significant drop in δL_p^* which can be inferred by analysing $\theta_\eta^2(\xi)$ and $\theta_\eta^4(\xi)$ (Fig. 25 and Fig. 28 respectively). The intermediate configuration between BPD II and BPD IV implies that ξ_1^*=0.3 and it achieves 67% stress reduction when the II mode is excited and 62% for the IV mode excitation.

Recently, a novel system based on a wireless power transfer has been developed to control PZT actuators mounted on rotating blades. The awareness of the optimal potential distributions is necessary to automatically maximise the efficiency of this system and reduce the stress on the blades as much as possible, whenever a resonant condition is met. It is worth noting that the proposed potential distribution method can be applied for any type of turbomachinery stage, other than the compressor and turbine stages, where the temperature exceeds 300 - 350°C, which corresponds to the Curie temperature of piezoceramics. Regardless of the machine or stage, it is possible to predict the potential distribution by exploiting the interference diagram (Section 3.1), for which the resonance conditions are likely to be the most detrimental. Such conditions are related to the rotational speed, structural characteristics and nature of the flow disturbances (i.e. inlet flow distortion generated by the presence of struts, non-uniformity of inlet ducts, inlet guide vanes, geometric asymmetries that occur during the bladed disc assembly, etc. [4, 5]). Usually, small EOs excite lower modes whereas high EOs, originating from the flow interaction between the rotor and stator blades of adjacent stages, excite higher modes. Nevertheless, the proposed model has a general application because once the excited modes and their shapes ($\theta_\eta^i(\xi)$) are identified, it is possible to analytically determine the optimal voltage distribution by knowing the position of their nodal lines. In other words, the optimal voltage distribution can be obtained by switching the electric potential sign in correspondence with each nodal line, regardless of the blade geometry.

Journal Pre-proof

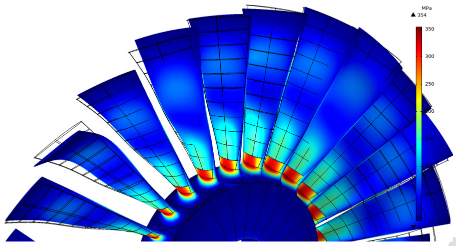

(a)

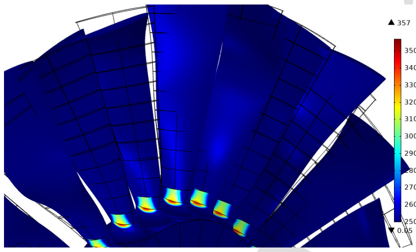

(b)

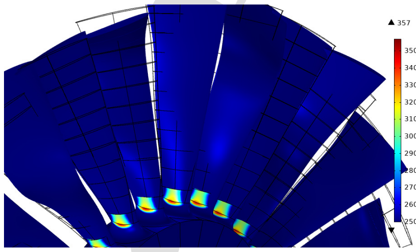

(c)

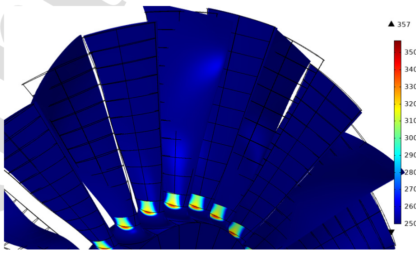

(d)

Figure 29: Total von Mises stress (MPa) calculated considering: (a) the total load: pre-load and harmonic pressures at 6EO forcing frequency (deactivated PZTs), (b) activation of the potential distribution C, (c) the potential distribution D and (d) the BPD IV.

5. Conclusions

A new piezoelectric active system for the mitigation of turbomachinery blades stress at resonance has been presented herein. The system relies on a model that determines the optimal voltage distribution on arrays of PZT actuator pairs, which has been extended here for the case of turbomachinery blades. The proposed model includes the effects of pre-twisting, non-constant cross-section area and the inertial loads of rotating blades, which restrict the decoupling of the flexural, torsional and extensional deformations. The kinematics of twisted blades and the inertial loads of rotating blades are derived in the Appendices. The advantages of the proposed model are two-fold: the possibility of identifying the optimal voltage distribution by analysing the nodal lines of the excited mode (or modes) and the exploitation of the flexural-torsional coupling to mitigate the torsional vibrations using the bending moments exerted by the PZT actuators. The results are not restricted to the type of blades considered in this paper but can be applied to any type of turbomachinery blade. Numerical FEA and CFD simulations on an axial fan stage coupled with a three-strut front frame have been performed to validate the model predictions in practical application, but the model can be applied for any bladed disc. High blade stress mitigation can be obtained for each resonance condition and the proposed model appears to be robust because there are several configurations close to optimal one that do not depress the stress relief effectiveness.

Appendix A Kinematics of twisted blades

Figure A.30(a) shows an undeformed pre-twisted blade, while in Fig. A.30(b) both the undeformed and deformed blade are depicted together with the local reference system and twist angle β:

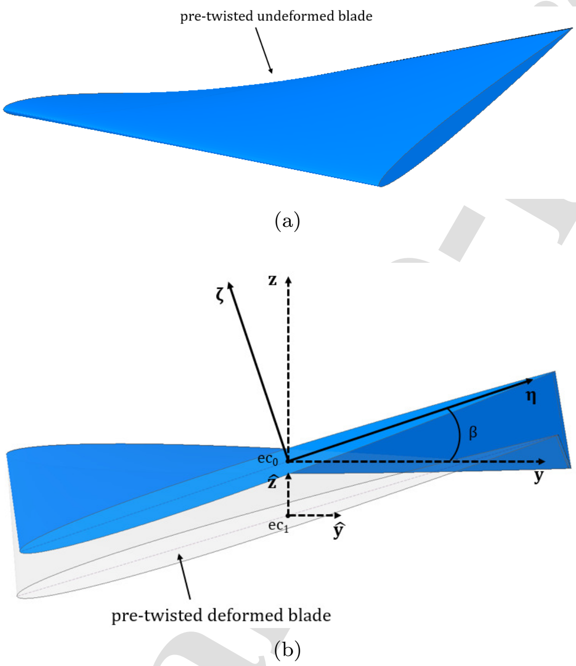

Figure A.30: (a) undeformed pre-twisted blade, (b) deformed pre-twisted blade local reference system. β is the blade twist angle.

The blade will deform because of the aerodynamic forces. In this paper, such motions will be analysed under the linear theory of elasticity, where only small displacements are considered, and the typical beam theory is used, where the cross-sections can be assumed as rigid (the warping is not considered). According to this theory, the motion of the section can be decomposed into a sum of translational and rotational motion. Choosing a reference system with the origin in the elastic centre (Fig. A.31(a)), the translational motion can be represented by the displacement of the origin $\mathbf{s}_{ec}$, which moves ec from ec_0 to ec_1 and the generic point P from P_0 to P_1. Considering ec_1, the origin of a new reference system $\{ec_1, \hat{x}, \hat{y}, \hat{z}\}$ used to describe the rotational motion and considering that the rotational motions can itself be decomposed into a first rotation θ_x with respect to the x axis, which moves P from P_1 to P_2 and the other two rotations $\{\theta_y, \theta_z\}$ that move such a point in P_3 out of the $\{y, z\}$ plane, as a consequence $\hat{\mathbf{s}}_P$ represents the rotatory component of the displacement (Fig. A.31(b)).

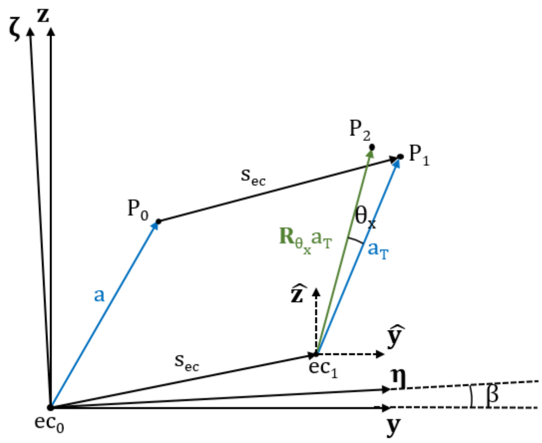

(a)

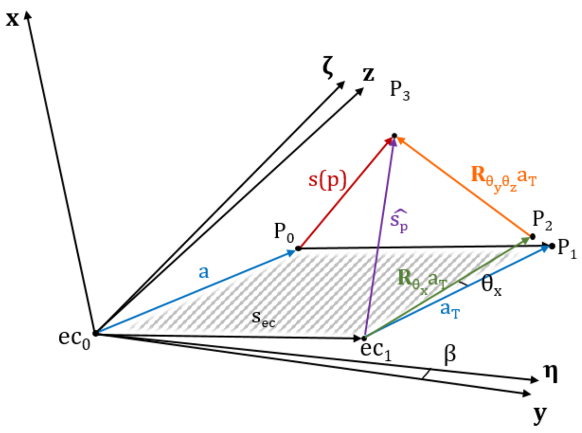

(b)

Figure A.31: Reference systems for the kinematics of twisted blades: (a) planar motions (translational + rotation around x-axis), and (b) out-of-plane rotations and total displacement vector $\mathbf{s}(P)$ representation.

To analytically describe this motion, it is necessary to use a vector $\boldsymbol{a}_T$, that locates the position of the point P in the $\{ec_1, \hat{x}, \hat{y}, \hat{z}\}$ reference system. If $\{0, \eta_P, \zeta_P\}$ are the components of the point P in the $\{\xi, \eta, \zeta\}$ reference system,
535 the components of the vector $\boldsymbol{a}_T$ in the $\{\hat{x}, \hat{y}, \hat{z}\}$ axis system will be:

$$\mathbf{a}_T = \begin{bmatrix} 1 & 0 & 0 \\ 0 & \cos(\beta) & -\sin(\beta) \\ 0 & \sin(\beta) & \cos(\beta) \end{bmatrix} \begin{Bmatrix} 0 \\ \eta_P \\ \zeta_P \end{Bmatrix} \tag{A.1}$$

considering the first rotation θ_x, $\mathbf{a}_T$ turns into $\mathbf{R}_{\theta_x}\mathbf{a}_T$:

$$\mathbf{R}_{\theta_x}\mathbf{a}_T = \begin{bmatrix} 1 & 0 & 0 \\ 0 & \cos(\beta+\theta_x) & -\sin(\beta+\theta_x) \\ 0 & \sin(\beta+\theta_x) & \cos(\beta+\theta_x) \end{bmatrix} \begin{Bmatrix} 0 \\ \eta_P \\ \zeta_P \end{Bmatrix} \tag{A.2}$$

For small rotations, θ_x can be rewritten as:

$$\mathbf{R}_{\theta_x}\mathbf{a}_T = \begin{bmatrix} 1 & 0 & 0 \\ 0 & \cos(\beta) - \theta_x \ \sin(\beta) & -\sin(\beta) - \theta_x \ \cos(\beta) \\ 0 & \sin(\beta) + \theta_x \ \cos(\beta) & \cos(\beta) - \theta_x \ \sin(\beta) \end{bmatrix} \begin{Bmatrix} 0 \\ \eta_P \\ \zeta_P \end{Bmatrix} = \begin{Bmatrix} 0 \\ y - \theta z \\ z + \theta y \end{Bmatrix} \tag{A.3}$$

Finally, applying the rotations $\{\theta_y$ and $\theta_z\}$ and introducing the corresponding matrix:

$$\mathbf{R}_{\theta_y\theta_z} = \begin{bmatrix} 1 & \theta_z & -\theta_y \\ -\theta_z & 1 & 0 \\ \theta_y & 0 & 1 \end{bmatrix} \tag{A.4}$$

540 the vector $\hat{\mathbf{s}}_P$ can be obtained, which, neglecting the second order terms,

can be expressed as:

$$\overset{\wedge}{\mathbf{s}}_P = \begin{bmatrix} 1 & \theta_z & -\theta_y \\ -\theta_z & 1 & 0 \\ \theta_y & 0 & 1 \end{bmatrix} \begin{Bmatrix} 0 \\ y - \theta_x z \\ z + \theta_x y \end{Bmatrix} = \begin{Bmatrix} \theta_z y - \theta_y z \\ y - \theta_x z \\ z + \theta_x y \end{Bmatrix} \tag{A.5}$$

Since:

$$\begin{cases} y = \eta \cos(\beta) - \zeta \sin(\beta) \\ z = \eta \sin(\beta) + \zeta \cos(\beta) \end{cases} \tag{A.6}$$

Eq. (A.5) becomes:

$$\overset{\wedge}{\mathbf{s}}_P = \begin{Bmatrix} \eta \Big[\theta_z \cos(\beta) - \theta_y \sin(\beta)\Big] - \zeta \Big[\theta_y \cos(\beta) + \theta_z \sin(\beta)\Big] \\ y - \theta_x z \\ z + \theta_x y \end{Bmatrix} \tag{A.7}$$

Considering that the rotation matrix between the reference system (1) $\{\hat{x}, \hat{y}, \hat{z}\}$ and the local reference system (2) $\{\hat{x}, \eta, \zeta\}$ is:

$$\mathbf{R}_{12} = \begin{bmatrix} 1 & 0 & 0 \\ 0 & \cos(\beta) & \sin(\beta) \\ 0 & -\sin(\beta) & \cos(\beta) \end{bmatrix} \tag{A.8}$$

The rotations $\{\theta_y, \theta_z\}$ in the reference system $\{\hat{x}, \eta, \zeta\}$ can be written as:

$$\begin{Bmatrix} 0 \\ \theta_\eta \\ \theta_\zeta \end{Bmatrix} = \mathbf{R}_{12} \mathbf{R}_{\theta_y \theta_z} \mathbf{R}_{12}^{-1} = \begin{Bmatrix} 0 \\ \theta_y \cos(\beta) + \theta_z \sin(\beta) \\ \theta_z \cos(\beta) - \theta_y \sin(\beta) \end{Bmatrix} \tag{A.9}$$

then $\overset{\wedge}{\mathbf{s}}_P$ simplifies into:

$$\overset{\wedge}{\mathbf{s}}_P = \begin{Bmatrix} \eta\theta_\zeta - \zeta\theta_\eta \\ y - \theta_x z \\ z + \theta_x y \end{Bmatrix} \tag{A.10}$$

Assuming the Euler-Bernoulli hypothesis (i.e., negligible shear deformation), the rotations $\theta_\eta, \theta_\zeta$ can be written as:

$$\begin{cases} \theta_\eta = -\gamma^I \\ \theta_\zeta = \alpha^I \end{cases} \tag{A.11}$$

where α and γ are the components of the displacement of the elastic centre in η and ζ directions, the superscript ^{I} denotes the differentiation with respect to x and Eq. (A.10) can also be rewritten in the following form:

$$\overset{\wedge}{\mathbf{s}}_P = \begin{Bmatrix} \eta\alpha^I + \zeta\gamma^I \\ y - \theta_x z \\ z + \theta_x y \end{Bmatrix} \tag{A.12}$$

If, instead, u, v and w represent the displacement components of the elastic centre in the $\{x, y, z\}$ reference system, then:

$$\mathbf{s}_{ec} = u\mathbf{i} + v\mathbf{j} + w\mathbf{k} \tag{A.13}$$

considering that:

$$\mathbf{s}(\mathbf{p}) = \mathbf{s}_{ec} + \overset{\wedge}{\mathbf{s}}_P \tag{A.14}$$

It is possible to obtain the components of the total displacement $\mathbf{s}(\mathbf{p})$:

$$\overset{\wedge}{\mathbf{s}}_P = \begin{Bmatrix} u + \eta\alpha^I + \zeta\gamma^I \\ v + y - \theta_x z \\ w + z + \theta_x y \end{Bmatrix} \tag{A.15}$$

Then it is possible to derive the strain ε_{xx} ([54], [55]):

$$\varepsilon_{xx} = u^I + \eta\alpha^{II} + \zeta\gamma^{II} + (\zeta^2 + \eta^2)\beta^I\theta_x^I \tag{A.16}$$

With χ the curvature with regard to η and ζ axes can be obtained:

$$\begin{cases} \chi_\zeta = \alpha^{II} \\ \chi_\eta = -\gamma^{II} \end{cases} \tag{A.17}$$

and

$$\chi_x = \theta_x^I \tag{A.18}$$

The (A.16) simplifies into:

$$\varepsilon_{xx} = u^I - \zeta\chi_\eta + \eta\chi_\zeta + (\zeta^2 + \eta^2)\beta^I\chi_x \tag{A.19}$$

and consequently:

$$\sigma_{xx} = E\varepsilon_{xx} = E\big[u^I - \zeta\chi_\eta + \eta\chi_\zeta + (\zeta^2 + \eta^2)\beta^I\chi_x\big] \tag{A.20}$$

If the M_η, M_ζ and M_x are the internal elastic moments, then:

$$\begin{cases} M_\eta = -\int_{\eta_{te}}^{\eta_{le}} \int_{-t/2}^{t/2} \sigma_{xx}\zeta \mathrm{d}\eta\mathrm{d}\zeta \\ M_\zeta = -\int_{\eta_{te}}^{\eta_{le}} \int_{-t/2}^{t/2} \sigma_{xx}\eta \mathrm{d}\eta\mathrm{d}\zeta \\ M_x = GJ\theta_x^I + \int_{\eta_{te}}^{\eta_{le}} \int_{-t/2}^{t/2} \sigma_{xx}(\beta + \theta_x)^I(\eta^2 + \zeta^2)\mathrm{d}\eta\mathrm{d}\zeta \end{cases} \tag{A.21}$$

Using the (A.20) their explicit expression can be evaluated and M_η can be expressed as:

$$M_\eta \quad = E\Bigg\{-u^I \int_{\eta_{te}}^{\eta_{le}} \int_{-t/2}^{t/2} \zeta \mathrm{d}\eta \mathrm{d}\zeta + \chi_\eta \int_{\eta_{te}}^{\eta_{le}} \int_{-t/2}^{t/2} \zeta^2 \mathrm{d}\eta \mathrm{d}\zeta - \chi_\zeta \int_{\eta_{te}}^{\eta_{le}} \int_{-t/2}^{t/2} \eta\zeta \mathrm{d}\eta \mathrm{d}\zeta + \\ -\beta^I \chi_x \int_{\eta_{te}}^{\eta_{le}} \int_{-t/2}^{t/2} \zeta(\zeta^2+\eta^2) \mathrm{d}\eta \mathrm{d}\zeta \Bigg\} \tag{A.22}$$

So long as the centre of gravity G lies on the η-axis and for section symmetry with respect to the same axis (Fig. A.31(a)), we can write:

$$\begin{cases} \int_{\eta_{te}}^{\eta_{le}} \int_{-t/2}^{t/2} \zeta \mathrm{d}\eta \mathrm{d}\zeta = 0 \\ \int_{\eta_{te}}^{\eta_{le}} \int_{-t/2}^{t/2} \eta\zeta \mathrm{d}\eta \mathrm{d}\zeta = 0 \\ \int_{\eta_{te}}^{\eta_{le}} \int_{-t/2}^{t/2} \zeta(\zeta^2+\eta^2) \mathrm{d}\eta \mathrm{d}\zeta = 0 \end{cases} \tag{A.23}$$

so that:

$$M_\eta = E I_\eta \chi_\eta \tag{A.24}$$

where

$$I_\eta = \int_{\eta_{te}}^{\eta_{le}} \int_{-t/2}^{t/2} \zeta^2 \mathrm{d}\eta \mathrm{d}\zeta \tag{A.25}$$

In a similar way M_ζ can be evaluated as:

$$M_\zeta \quad = E\Bigg\{-u^I \int_{\eta_{te}}^{\eta_{le}} \int_{-t/2}^{t/2} \eta \mathrm{d}\eta \mathrm{d}\zeta + \chi_\eta \int_{\eta_{te}}^{\eta_{le}} \int_{-t/2}^{t/2} \eta\zeta \mathrm{d}\eta \mathrm{d}\zeta - \chi_\zeta \int_{\eta_{te}}^{\eta_{le}} \int_{-t/2}^{t/2} \eta^2\zeta \mathrm{d}\eta \mathrm{d}\zeta + \\ -\beta^I \chi_x \int_{\eta_{te}}^{\eta_{le}} \int_{-t/2}^{t/2} \eta(\zeta^2+\eta^2) \mathrm{d}\eta \mathrm{d}\zeta \Bigg\} \tag{A.26}$$

570 with:

$$\begin{cases} I_\zeta = \int_{\eta_{te}}^{\eta_{le}} \int_{-t/2}^{t/2} \eta^2 \mathrm{d}\eta \mathrm{d}\zeta \\ B_\zeta = \int_{\eta_{te}}^{\eta_{le}} t\eta(\eta^2 + \frac{t^2}{12}) \mathrm{d}\eta \\ e_A = \frac{1}{A} \int_{\eta_{te}}^{\eta_{le}} \int_{-t/2}^{t/2} \eta \mathrm{d}\eta \mathrm{d}\zeta \end{cases} \tag{A.27}$$

Taking into account the symmetry of the section with respect to η-axis, we can write:

$$M_\zeta = -EI_\zeta \chi_\zeta - EB_\zeta \beta^I \chi_x - EAe_A u^I \tag{A.28}$$

Proceeding in the same way for M_x, we obtain the following:

$$\begin{aligned} M_x \quad &= GJ\theta_x^I + E(\beta^I + \theta_x^I) \Bigg\{ -u^I \int_{\eta_{te}}^{\eta_{le}} \int_{-t/2}^{t/2} (\zeta^2 + \eta^2) \mathrm{d}\eta \mathrm{d}\zeta - \chi_\eta \int_{\eta_{te}}^{\eta_{le}} \int_{-t/2}^{t/2} \zeta (\zeta^2 + \eta^2) \mathrm{d}\eta \mathrm{d}\zeta + \\ &+ \chi_\zeta \int_{\eta_{te}}^{\eta_{le}} \int_{-t/2}^{t/2} \eta (\zeta^2 + \eta^2) \mathrm{d}\eta \mathrm{d}\zeta - \beta^I \chi_x \int_{\eta_{te}}^{\eta_{le}} \int_{-t/2}^{t/2} \eta (\zeta^2 + \eta^2)^2 \mathrm{d}\eta \mathrm{d}\zeta \Bigg\} \end{aligned} \tag{A.29}$$

with the following definitions:

$$\begin{cases} H_0 = \int_{\eta_{te}}^{\eta_{le}} \int_{-t/2}^{t/2} (\zeta^2 + \eta^2)^2 \mathrm{d}\eta \mathrm{d}\zeta \\ k_A = \sqrt{\frac{1}{A} \int_{\eta_{te}}^{\eta_{le}} \int_{-t/2}^{t/2} (\zeta^2 + \eta^2) \mathrm{d}\eta \mathrm{d}\zeta} \end{cases} \tag{A.30}$$

575 Eq. A.29 turns into:

$$M_x = GJ\chi_x + E(\beta^I + \chi_x) \Big[Ak_A^2 u^I + B_\zeta \chi_\zeta + H_0 \beta^I \chi_x \Big] \tag{A.31}$$

Appendix B Inertial loads of rotating blades

The calculus of the inertia loads can be facilitated through the introduction of the inertial reference system $\{X, Y, Z\}$, resulting in the following:

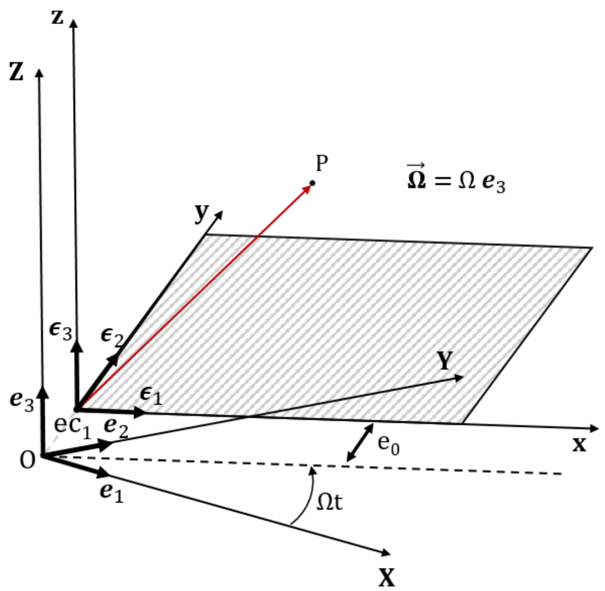

Figure B.32: Inertial (X,Y,Z) and local (x,y,z) reference system.

The position of the generic point P, in the two reference systems $\{X, Y, Z\}$
580 and $\{x, y, z\}$ is identified by:

$$\mathbf{OP}(t) = X_P(t)\mathbf{e}_1 + Y_P(t)\mathbf{e}_2 + Z_P(t)\mathbf{e}_3 = x_P(t)\boldsymbol{\epsilon}_1(t) + y_P(t)\boldsymbol{\epsilon}_2(t) + z_P(t)\mathbf{e}_3 \quad \text{(B.1)}$$

where $x_P(t), y_P(t), z_P(t)$ can be obtained by the (A.13)-(A.15):

$$\begin{cases} x_P(t) = x_0 + u(t) + \eta\alpha^I(t) + \zeta\gamma^I(t) \\ y_P(t) = y_0 + v(t) - z_0\theta_x(t) + e_0 \\ z_P(t) = z_0 + w(t) + y_0\theta_x(t) \end{cases} \quad \text{(B.2)}$$

The first derivative with respect to time gives the velocity field:

$$\dot{\mathbf{OP}}(t) = \dot{X}_P(t)\mathbf{e}_1 + \dot{Y}_P(t)\mathbf{e}_2 + \dot{Z}_P(t)\mathbf{e}_3 =$$
$$= \dot{x}_P(t)\boldsymbol{\epsilon}_1(t) + x_P(t)\dot{\boldsymbol{\epsilon}}_1(t) + \dot{y}_P(t)\boldsymbol{\epsilon}_2(t) + y_P(t)\dot{\boldsymbol{\epsilon}}_2(t) + \dot{z}_P(t)\mathbf{e}_3 \quad \text{(B.3)}$$

We must also consider the following:

$$\boldsymbol{\Omega} = \Omega \mathbf{e}_3 \quad \text{(B.4)}$$

and

$$\begin{cases} \dot{\boldsymbol{\epsilon}}_1(t) = \Omega \boldsymbol{\epsilon}_2 \\ \dot{\boldsymbol{\epsilon}}_2(t) = -\Omega \boldsymbol{\epsilon}_1 \end{cases} \quad \text{(B.5)}$$

This can be simplified to obtain:

$$\dot{\mathbf{OP}}(t) = \left[\dot{x}_P(t) - \Omega y_P(t)\right]\boldsymbol{\epsilon}_1 + \left[\dot{y}_P(t) + \Omega x_P(t)\right]\boldsymbol{\epsilon}_2 + \dot{z}_P(t)\mathbf{e}_3 \quad \text{(B.6)}$$

The second derivative gives the acceleration field:

$$\ddot{\mathbf{OP}}(t) = \ddot{X}_P(t)\mathbf{e}_1 + \ddot{Y}_P(t)\mathbf{e}_2 + \ddot{Z}_P(t)\mathbf{e}_3 = \left[\ddot{x}_P(t) - 2\Omega\,\dot{y}_P(t) - \Omega^2 x_P(t)\right]\boldsymbol{\epsilon}_1 +$$
$$+ \left[\ddot{y}_P(t) - 2\Omega\,\dot{x}_P(t) - \Omega^2 y_P(t)\right]\boldsymbol{\epsilon}_2 + \ddot{z}_P(t)\mathbf{e}_3 \quad \text{(B.7)}$$

The derivative of $x_P(t), y_P(t)$ and $z_P(t)$ can be written considering (B.2):

$$\begin{cases} \dot{x}_P(t) = \dot{u}(t) + \eta\,\dot{\alpha}^I(t) + \zeta\,\dot{\gamma}^I(t) \\ \dot{y}_P(t) = \dot{v}(t) - z_0\,\dot{\theta}_x(t) \\ \dot{z}_P(t) = \dot{w}(t) + y_0\,\dot{\theta}_x(t) \end{cases} \quad \text{(B.8)}$$

$$
\begin{cases}
\ddot{x}_P\ (t) = \ddot{u}\ (t) + \eta\ \ddot{\alpha}^I\ (t) + \zeta\ \ddot{\gamma}^I\ (t) \\
\ddot{y}_P\ (t) = \ddot{v}\ (t) - z_0\ \ddot{\theta}_x\ (t) \\
\ddot{z}_P\ (t) = \ddot{w}\ (t) + y_0\ \ddot{\theta}_x\ (t)
\end{cases}
\tag{B.9}
$$

Then, it is possible to obtain the components a_x, a_y, a_z of the acceleration in the local reference system $\{x, y, z\}$, since they are necessary to calculate the

590 inertial loads in (3):

$$
\begin{cases}
a_x(x,t) = \ddot{u}\ (t) + \eta\ \ddot{\alpha}^I\ (t) + \zeta\ \ddot{\gamma}^I\ (t) - 2\Omega\Big[\ \dot{v}\ (t) - z_0\ \dot{\theta}_x\ (t)\Big] \\
-\Omega^2\Big[x_0 + u(t) + \eta\alpha^I(t) + \zeta\gamma^I(t)\Big] \\
a_y(x,t) = \ddot{v}\ (t) - z_0\ \ddot{\theta}_x\ (t) - 2\Omega\Big[\ \dot{u}\ (t) + \eta\ \dot{\alpha}^I\ (t) + \zeta\ \dot{\gamma}^I\ (t)\Big] \\
-\Omega^2\Big[y_0 + v(t) - z_0\theta_x(t) + e_0\Big] \\
a_z(x,t) = \ddot{w}\ (t) + y_0\ \ddot{\theta}_x\ (t)
\end{cases}
\tag{B.10}
$$

For the purpose of calculating the inertial loads in (3) it is convenient to write (B.10) as a function of x, η, ζ:

$$
\begin{cases}
a_x(x,t) = \ddot{u}\ (x,t) + \eta\ \ddot{\alpha}^I\ - \zeta\ \ddot{\theta}_\eta\ (x,t) - 2\Omega\left\{\dot{v}\ (x,t) + \dot{\theta}_x\ (x,t)\left[\zeta\cos(\beta) + \eta\sin(\beta)\right]\right\} \\
-\Omega^2\Big[x_0 + u(x,t) + \eta\alpha^I(x,t) + \zeta\gamma^I(x,t)\Big] \\
a_y(x,t) = \ddot{v}\ (t) - \ddot{\theta}_x\ (t)\Big[\zeta\cos(\beta) + \eta\sin(\beta)\Big] - 2\Omega\Big[\ \dot{u}\ (t) + \eta\ \dot{\alpha}^I\ (t) + \zeta\ \dot{\gamma}^I\ (t)\Big] \\
-\Omega^2\Big\{\eta\cos(\beta) - \zeta\sin(\beta) + v(t) - \big[\zeta\cos(\beta) + \eta\sin(\beta)\big]\theta_x(t) + e_0\Big\} \\
a_z(x,t) = \ddot{w}\ (x,t) + \ddot{\theta}_x\ (x,t)\Big[\eta\cos(\beta) - \zeta\sin(\beta)\Big]
\end{cases}
\tag{B.11}
$$

Then, we write the components of the acceleration in the $\{x, \eta, \zeta\}$ reference system:

$$\begin{Bmatrix} a_x(x,t) \\ a_\eta(x,t) \\ a_\varsigma(x,t) \end{Bmatrix} = \mathbf{R}_{12} \begin{Bmatrix} a_x(x,t) \\ a_y(x,t) \\ a_z(x,t) \end{Bmatrix} \tag{B.12}$$

595 The inertial loads $p_x^{in}, p_\eta^{in}, p_\zeta^{in}$, per unit length, will be (Fig. B.33):

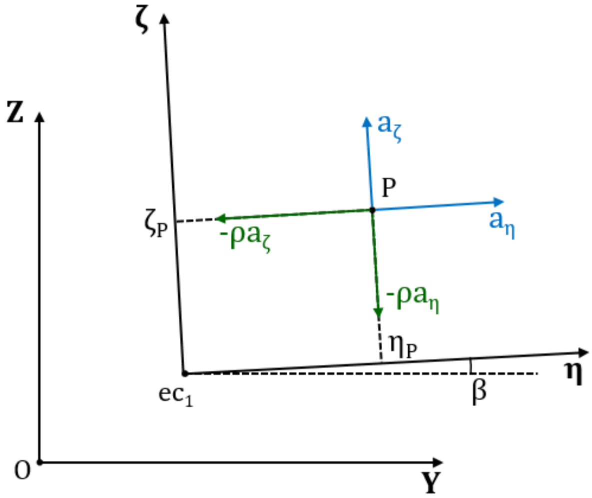

Figure B.33: Inertial loads illustration in (ζ, η) plane.

$$\begin{cases} p_x^{in}(x,t) = -\rho \int_{\eta_{te}}^{\eta_{le}} \int_{-t/2}^{t/2} a_x \mathrm{d}\eta \mathrm{d}\zeta \\ p_\eta^{in}(x,t) = -\rho \int_{\eta_{te}}^{\eta_{le}} \int_{-t/2}^{t/2} a_\eta \mathrm{d}\eta \mathrm{d}\zeta \\ p_\zeta^{in}(x,t) = -\rho \int_{\eta_{te}}^{\eta_{le}} \int_{-t/2}^{t/2} a_\varsigma \mathrm{d}\eta \mathrm{d}\zeta \end{cases} \tag{B.13}$$

The inertial moments will be:

$$\begin{cases} q_x^{in}(x,t) = -\rho \int_{\eta_{te}}^{\eta_{le}} \int_{-t/2}^{t/2} (-a_\eta \zeta + a_\varsigma \eta) \mathrm{d}\eta \mathrm{d}\zeta \\ q_\eta^{in}(x,t) = -\rho \int_{\eta_{te}}^{\eta_{le}} \int_{-t/2}^{t/2} a_x \zeta \mathrm{d}\eta \mathrm{d}\zeta \\ q_\zeta^{in}(x,t) = -\rho \int_{\eta_{te}}^{\eta_{le}} \int_{-t/2}^{t/2} -a_x \eta \mathrm{d}\eta \mathrm{d}\zeta \end{cases} \tag{B.14}$$

Appendix C Aerodynamic loads

The resultant $p_a(t)$ of the aerodynamic pressure acting on the edge of a generic airfoil can be calculated as:

$$p_a(t) = \oint_{\ell} P_a(t)\mathrm{d}\ell \tag{C.1}$$

where $P_a(t)$ is the pressure acting on the blade surfaces (Fig. C.34) obtained using CFD simulation in Section 3.2.

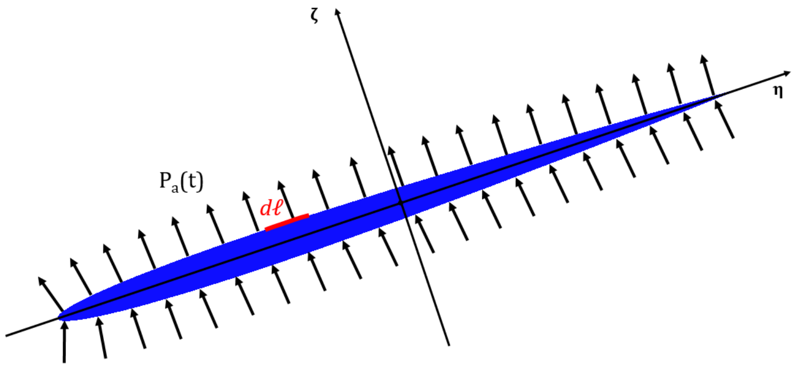

Figure C.34: $P_a(t)$ pressure acting on the edge of an airfoil of the blade.

The resultant of the moments due to the aerodynamic loads can be written as:

$$q_a(t) = \oint_{\ell} \eta P_a(t)\mathrm{d}\ell \tag{C.2}$$

Finally, the virtual work of the aerodynamic loads can be obtained by considering both the $p_a(t)$ and $q_a(t)$ contributions:

$$\delta L_a = \int_0^L (p_a \stackrel{\sim}{\gamma} + q_a \stackrel{\sim}{\theta}_x)\mathrm{d}x \tag{C.3}$$

References

[1] E. Poursaeidi, H. Bakhtiari, Fatigue crack growth simulation in a first stage of compressor blade, Eng. Fail. Anal. 45 (2014) 314–325. doi:10.1016/j.engfailanal.2014.06.018.

[2] L. Witek, Experimental crack propagation and failure analysis of the first stage compressor blade subjected to vibration, Eng. Fail. Anal. 16 (7) (2009) 2163–2170. doi:10.1016/j.engfailanal.2009.02.014.

[3] J. Li, N. Aye-Addo, N. Kormanik, D. Matthews, N. Key, R. Kielb, Mistuned higher-order mode forced response of an embedded compressor rotor: Part i—steady and unsteady aerodynamics, in: ASME Turbo Expo 2017: Turbomachinery Technical Conference and Exposition, American Society of Mechanical Engineers Digital Collection, 2017.

[4] A. Sayma, M. Vahdati, M. Imregun, An integrated nonlinear approach for turbomachinery forced response prediction. part i: Formulation, J. Fluid Struct. 14 (1) (2000) 87–101. doi:10.1006/jfls.1999.0253.

[5] M. Vahdati, A. Sayma, M. Imregun, An integrated nonlinear approach for turbomachinery forced response prediction. part ii: Case studies, J. Fluid Struct. 14 (1) (2000) 103–125. doi:10.1006/jfls.1999.0254.

[6] G. Sharma, L. Zori, S. Connell, P. Godin, Efficient computation of large pitch ratio transonic flow in a fan with inlet distortion, in: Turbo Expo: Power for Land, Sea, and Air, Vol. 55249, American Society of Mechanical Engineers, 2013, p. V06CT42A025.

[7] Z. X. Liu, H. Z. Diao, X. C. Zhu, Z. H. Du, Numerical investigation of the axial compressor performance with inlet distortions, Proceedings of the Institution of Mechanical Engineers, Part G: Journal of Aerospace Engineering 232 (8) (2018) 1434–1441. doi:10.1177/0954410017699853.

[8] K. Yamamoto, W. F. Ng, The development of flow distortions at the fan face for an axisymmetric supersonic inlet, J. Sound Vib. 203 (1) (1997) 75–85. doi:10.1006/jsvi.1996.0763.

[9] A. R. Wadia, P. N. Szucs, Inner workings of shrouded and un-shrouded transonic fan blades, J. Turbomach. 130(3) (Jul. 2008). doi:10.1115/1.2776957.

[10] W. B. Roberts, A Design Point Correlation for Losses due to Part-Span Dampers on Transonic Rotors, J. Eng. Power. 101 (3) (1979) 415–421. doi:10.1115/1.3446594.

[11] P. Neumann, V. B. C. de Almeida, V. Motta, L. Malzacher, D. Peitsch, G. Quaranta, Dynamic mode decomposition analysis of plasma aeroelastic control of airfoils in cascade, J. Fluid Struct. 94 (2020) 102901. doi:10.1016/j.jfluidstructs.2020.102901.

[12] V. C. de Sousa, T. M. P. Silva, C. D. M. Junior, Aeroelastic flutter enhancement by exploiting the combined use of shape memory alloys and nonlinear piezoelectric circuits, J. Sound Vib. 407 (2017) 46–62. doi:10.1016/j.jsv.2017.06.034.

[13] J. M. McCarthy, S. Watkins, A. Deivasigamani, S. J. John, Fluttering energy harvesters in the wind: A review, J. Sound Vib. 361 (2016) 355–377. doi:10.1016/j.jsv.2015.09.043.
URL https://ui.adsabs.harvard.edu/abs/2016JSV...361..355M

[14] P. Alevras, S. Theodossiades, Vibration energy harvester for variable speed rotor applications using passively self-tuned beams, J. Sound Vib. 444 (2019) 176–196. doi:10.1016/j.jsv.2018.11.007.
URL https://ui.adsabs.harvard.edu/abs/2019JSV...444..176A

[15] J. Xiang, Y. Wu, D. Li, Energy harvesting from the discrete gust response of a piezoaeroelastic wing: Modeling and performance evaluation, J. Sound Vib. 343 (2015) 176–193. doi:https:

//doi.org/10.1016/j.jsv.2014.12.023.
URL https://www.sciencedirect.com/science/article/pii/S0022460X1401027X

[16] X. Wang, P. Xia, P. Masarati, Active aeroelastic control of aircraft wings with piezo-composite, J. Sound Vib. 455 (2019) 1–19. doi:https://doi.org/10.1016/j.jsv.2019.04.035.
URL https://www.sciencedirect.com/science/article/pii/S0022460X19302548

[17] S. Na, J.-S. Song, J.-H. Choo, Z. Qin, Dynamic aeroelastic response and active control of composite thin-walled beam structures in compressible flow, J. Sound Vib. 330 (21) (2011) 4998–5013. doi:https://doi.org/10.1016/j.jsv.2011.05.026.
URL https://www.sciencedirect.com/science/article/pii/S0022460X11004111

[18] Y. Yi, W. Seemann, R. Gausmann, J. Zhong, A method for matching the eigenfrequencies of longitudinal and torsional vibrations in a hybrid piezoelectric motor, J. Sound Vib. 295 (3) (2006) 856–869. doi:https://doi.org/10.1016/j.jsv.2006.01.043.
URL https://www.sciencedirect.com/science/article/pii/S0022460X06001404

[19] C. J. Cross, S. Fleeter, Shunted piezoelectrics for passive control of turbomachine blading flow-induced vibrations, Smart Mater. Struct. 11 (2) (2002) 239. doi:10.1088/0964-1726/11/2/307.

[20] J. Min, K. Duffy, B. Choi, C. Morrison, R. Jansen, A. Provenza, A resonant damping study using piezoelectric materials, in: 49th AIAA/ASME/ASCE/AHS/ASC Structures, Structural Dynamics, and Materials Conference, 16th AIAA/ASME/AHS Adaptive Structures Conference, 10th AIAA Non-Deterministic Approaches Conference, 9th AIAA

Gossamer Spacecraft Forum, 4th AIAA Multidisciplinary Design Optimization Specialists Conference, 2008, p. 2335.

[21] K. Duffy, A. Provenza, J. Trudell, J. Min, Passively shunted piezoelectric damping of centrifugally loaded plates, in: 50th AIAA/ASME/ASCE/AHS/ASC Structures, Structural Dynamics, and Materials Conference 17th AIAA/ASME/AHS Adaptive Structures Conference 11th AIAA No, 2009, p. 2524.

[22] I. Goltz, H. Böhmer, R. Nollau, J. Belz, B. Grüber, J. Seume, Piezo-electric actuation of rotor blades in an axial compressor, in: ETC 2009 - 8th European Conference on Turbomachinery, 2009.

[23] B. Choi, C. Morrison, K. Duffy, An active damping at blade resonances using piezoelectric transducers, NASA/TM - 2008-215212 (2008).

[24] B. Choi, J. Kauffman, K. Duffy, A. Provenza, C. Morrison, Active vibration reduction of titanium alloy fan blades (fan1) using piezoelectric materials, NASA/TM - 2010-216335 (2010).

[25] A. J. Provenza, C. R. Morrison, Control of fan blade vibrations using piezoelectrics and bi-directional telemetry, in: ASME 2011 Turbo Expo: Turbine Technical Conference and Exposition, American Society of Mechanical Engineers Digital Collection, 2011, pp. 923–930.

[26] E. F. Crawley, J. De Luis, Use of piezoelectric actuators as elements of intelligent structures, AIAA J. 25 (10) (1987) 1373–1385. doi:10.2514/3.9792.

[27] J. Ducarne, O. Thomas, J. Deü, Placement and dimension optimization of shunted piezoelectric patches for vibration reduction, J. Sound Vib. 331 (14) (2012) 3286–3303. doi:10.1016/j.jsv.2012.03.002.

[28] F. Botta, A. Scorza, A. Rossi, Optimal piezoelectric potential distribution for controlling multimode vibrations, App. Sci. - Basel 8 (4) (2018) 551. doi:10.3390/app8040551.

[29] S. Moffatt, L. He, On decoupled and fully-coupled methods for blade forced response prediction, J. Fluid Struct. 20 (2005) 217–234. doi:10.1016/j.jfluidstructs.2004.10.012.

[30] F. Botta, N. Marx, C. Schwingshackl, G. Cerri, D. Dini, A wireless vibration control technique for gas turbine blades using piezoelectric plates and contactless energy transfer, in: ASME Turbo Expo 2013: Turbine Technical Conference and Exposition, American Society of Mechanical Engineers Digital Collection, 2013.

[31] C. Bréard, J. S. Green, M. Vahdati, M. Imregun, A non-linear integrated aeroelasticity method for the prediction of turbine forced response with friction dampers, Int. J. Mech. Sci. 43 (12) (2001) 2715–2736. doi:10.1016/S0020-7403(01)00074-1.

[32] K. Y. Sanliturk, D. J. Ewins, A. B. Stanbridge, Underplatform dampers for turbine blades: Theoretical modeling, analysis, and comparison with experimental data, ASME. J. Eng. Gas Turbines Power 123 (2001) 919–929. doi:10.1115/1.1385830.

[33] C. M. Firrone, S. Zucca, Underplatform dampers for turbine blades: The effect of damper static balance on the blade dynamics, Mech. Res. Commun. 36 (2009) 515–522. doi:0.1016/j.mechrescom.2009.01.002.

[34] F. Botta, A. Rossi, N. P. Belfiore, A novel method to fully suppress single and bi-modal excitations due to the support vibration by means of piezoelectric actuators, J. Sound Vib. 510 (2021) 116260. doi:10.1016/j.jsv.2021.116260.

[35] A. Rossi, F. Botta, R. Maiozzi, A. Scorza, S. A. Sciuto, Experimental results for active control of multimodal vibrations by optimally placed piezoelectric actuators, MATEC Web Conf., 211 (2018) 20001 211 (2018) 20001. doi:10.1051/matecconf/201821120001.

[36] F. Botta, A. Rossi, L. Schinaia, A. Scorza, F. Orsini, S. Sciuto, N. Belfiore, Experimental validation on optimal placement of pzt plates for active beam multimode vibrations reduction, in: AIMETA 2017 Proceedings of the 23rd Conference of the Italian Association of Theoretical and Applied Mechanics, Vol. 3, 2017, pp. 2258–2269.

[37] F. Botta, F. Toccaceli, Piezoelectric plates distribution for active control of torsional vibrations, Actuators 7 (2018) 23. doi:https://doi.org/10.3390/act7020023.

[38] I. Bruant, G. Coffignal, F. Lene, M. Verge, A methodology for determination of piezoelectric actuator and sensor location on beam structures, J. Sound Vib. 243 (5) (2001) 861–882. doi:10.1006/jsvi.2000.3448.

[39] K. D. Dhuri, P. Seshu, Piezo actuator placement and sizing for good control effectiveness and minimal change in original system dynamics, Smart Mater. Struct. 15 (6) (2006) 1661. doi:10.1088/0964-1726/15/6/019.

[40] K. R. Kumar, S. Narayanan, Active vibration control of beams with optimal placement of piezoelectric sensor/actuator pairs, Smart Mater. Struct. 17 (5) (2008) 055008. doi:10.1088/0964-1726/17/5/055008.

[41] H.-j. Kou, J.-s. Lin, J.-h. Zhang, Numerical study on vibration stress of rotating fan blade under aerodynamic load at critical speed, Proceedings of the Institution of Mechanical Engineers, Part G: Journal of Aerospace Engineering 230 (6) (2016) 1044–1058. doi:10.1177/0954410015603071.

[42] D. L. Thomas, Dynamics of rotationally periodic structures, Int. J. Numer. Meth. Eng. 14 (1) (1979) 81–102. doi:10.1002/nme.1620140107.

[43] P. Balasubramanian, J. G. Jagadeesh, H. K. Suhas, A. K. Srivastava, V. Ramamurti, On the use of the ritz-wilson method for the dynamic response analysis of cyclic symmetric structures, J. Sound Vib. 164 (2) (1993) 193–206. doi:10.1006/jsvi.1993.1208.

[44] M. P. Singh, J. J. Vargo, Reliability evaluation of shrouded blading using the safe interference diagram, J. Eng. Gas Turbines Power 111 (1989) 601–609. doi:10.1115/1.3240296.

[45] M. P. Singh, Safe diagram. st 16, Tech. rep., Dresser – Rand Company, (1984).

[46] L. Bertini, P. Neri, C. Santus, A. Guglielmo, G. Mariotti, Analytical investigation of the safe diagram for bladed wheels, numerical and experimental validation, J. Sound Vib. 333 (2014) 4771–4788. doi:10.1016/j.jsv.2014.04.061.

[47] ANSYS, CFX-Solver Theory Guide 19.2.

[48] D. Witteck, D. Micallef, R. Mailach, Comparison of transient blade row methods for the cfd analysis of a high-pressure turbine, in: Turbo Expo: Power for Land, Sea, and Air, Vol. 45639, American Society of Mechanical Engineers, 2014, p. V02DT44A020.

[49] F. R. Menter, Two-equation eddy-viscosity turbulence models for engineering applications, AIAA J. 32 (8) (1994) 1598–1605. doi:10.2514/3.12149.

[50] T. Biesinger, C. Cornelius, C. Rube, A. Braune, R. Campregher, P. G. Godin, G. Schmid, L. Zori, Unsteady cfd methods in a commercial solver for turbomachinery applications, in: Turbo Expo: Power for Land, Sea, and Air, Vol. 44021, 2010, pp. 2441–2452.

[51] T. Biesinger, C. Cornelius, D. Nürnberger, C. Rube, Speed line computation of a transonic compressor stage with unsteady cfd methods, in: Turbo Expo: Power for Land, Sea, and Air, Vol. 44748, American Society of Mechanical Engineers, 2012, pp. 1853–1862.

[52] C. Cornelius, T. Biesinger, P. Galpin, A. Braune, Experimental and computational analysis of a multistage axial compressor including stall prediction by steady and transient cfd methods, J. Turbomach. 136 (6) (2014). doi:10.1115/1.4025583.

[53] B. Winhart, D. Micallef, D. Engelmann, Application of the time-transformation method for a detailed analysis of multistage blade row interactions in a shrouded turbine, in: 12 th European Conference on Turbomachinery Fluid dynamics & Thermodynamics, EUROPEAN TURBOMACHINERY SOCIETY, 2017.

[54] J. C. Houbolt, G. W. Brooks, Differential equations of motion for combined flapwise bending, chordwise bending, and torsion of twisted nonuniform rotor blades, Vol. 1346, National Advisory Committee for Aeronautics, 1957.

[55] D. H. Hodges, E. H. Dowell, Nonlinear equations of motion for the elastic bending and torsion of twisted nonuniform rotor blades, NASA TN D-7818, 1974.

Highlights

- Resonance is one of the main roots of high cycle fatigue (HCF) in turbomachinery blades.
- Piezoelectric (PZT) actuators can be tuned up on each resonance to actively damp vibrations.
- An active piezoelectric system consisting of 10 PZT actuators pairs is considered to mitigate the blade stress.
- The optimal voltage distribution that implies the maximum stress reduction is investigated.
- Numerical CFD and FEA simulations have been performed to validate the model predictions.
- The proposed method allows to reach up to 70% blade stress mitigation for each resonance condition.

CRediT author statement

Andrea Rossi: Conceptualization, Software, Investigation, Data curation, Visualization, Writing- Original draft preparation. **Fabio Botta**: Conceptualization, Methodology, Investigation, Visualization, Writing- Original draft preparation. **Ambra Giovannelli**: Resources, Writing - Review & Editing, Supervision. **Nicola Pio Belfiore***:* Supervision, Writing - Review & Editing.